João Nuno Ferreira Barbosa

FERROMAGNETIC SPIN SYSTEMS PROBED IN MILLIKELVIN REGIME USING MICROWAVE SPECTROSCOPY

VOLUME 1

Janeiro de 2020

João Nuno Ferreira Barbosa

FERROMAGNETIC SPIN SYSTEMS PROBED IN MILLIKELVIN REGIME USING MICROWAVE SPECTROSCOPY

VOLUME 1

Janeiro de 2020

This work was developed at:

University of Glasgow, Scotland, UK

Acknowledgments

Since this section is supposed to be short, I will not individually thank every single person that has helped (in many different ways) in this journey, but instead begin by saying that I really am grateful for everyone who did. However, after these last two years and after completing this thesis, I really felt the need to talk about people without whom it would have been next to impossible to get this work done.

First, I thank my mother, father, sister and my (Dr.) cousin. What would I be without my family?

I am grateful for all the friends I have made over the last years, specially my three closest friends which I have known for more than 12 years and the great group of friends we "created" that has been growing with awesome people ever since ("ZGs")! Also, I cannot forget the friends I have made in university during this degree.

I also want to thank all professors I had during my time as a student in the university. Everyone has taught me something, from technical to personal skills, as well as stimulated my interest for physics and engineering (in one way or another!). I have yet to had a day in my life where I regretted choosing this degree and this area to work on. Special thanks to Prof. Fernando Nogueira who was one of few who noticed this interest and introduced me to the world of research.

Last, but not least, I am eternally grateful to Prof. Martin Weides (together with the ERASMUS+ programme) for accepting me into his group and allowing me to work on something I had only dreamt about before meeting him. I will forever appreciate his great supervision and leadership, the amazing research group he has created in Glasgow and the opportunity to keep working in this area in the upcoming years! Thanks Martin!

Resumo

Este trabalho envolveu o estudo de sistemas de spin ferromagnéticos, nomeadamente amostras de Yttrium Iron Garnet (YIG), através da observação e caracterização de fenómenos de ressonância ferromagnetica (FMR), utilizando espectroscopia de microondas. Este estudo foi realizado a temperatura ambiente com uma esfera e um filme fino de YIG, onde o objetivo passou por caracterizar as amostras e compará-las com resultados de literatura prévia, com especial atenção às perdas no sistema e os correspondentes fatores de amortecimento. Este estudo foi também realizado a temperaturas criogénicas com amostras de YIG fabricadas através de deposição com Plasma Focused Ion Beam (FIB), que foram posteriormente colocadas num Refrigerador de Desmagnetização Adiabática e arrefecidas até temperaturas de milliKelvin.

Utilizando esta técnica de fabricação, foi possível remover o substrato de Gallium Gadolinium Garnet (GGG), utilizado em filmes finos de YIG, que aumenta a largura da curva de ressonância ferromagnética a temperaturas milliKelvin, como foi demonstrado recentemente. De facto, os resultados apresentados mostram que a largura não aumenta a temperaturas de milliKelvin quando comparado com amostras a 3 K. Foi também possível testar um regime de acoplamento entre um ressoador supercondutor e as mesmas, onde o sistema híbrido cria um fenómeno de "avoided crossing". O espectro obtido mostra características de um sistema fracamente acoplado, onde o sistema magnónico atua como um canal de dissipação para os fotões microondas. Estas amostras, juntamente com o estudo das suas características e do sistema híbrido, são um passo relevante para futuras experiências na área de magnónica quântica.

Keywords: Engenharia de microondas; Ressonância ferromagnética; Regime milliKelvin; Circuitos híbridos quânticos; Magnónica quântica

Abstract

In this work, ferromagnetic spin systems were studied, namely Yttrium Iron Garnet (YIG) samples, by observing and characterising ferromagnetic resonance (FMR), using microwave spectroscopy. This study was performed at room temperature with a YIG sphere and thin film, where the objective was to characterise the samples and compare them to previous literature, with special attention to losses and the corresponding damping factors. The study was also performed at cryogenic temperatures with YIG samples fabricated using Plasma Focused Ion Beam (FIB) structuring and deposition, which were then placed inside an Adiabatic Demagnetization Refrigerator (ADR) and cooled down to milliKelvin temperatures.

Using this fabrication technique, it was possible to remove the Gallium Gadolinium Garnet (GGG) substrate commonly used in YIG thin films, which has been shown to increase the ferromagnetic resonance linewidth at milliKelvin temperatures. Indeed, our results show that the linewidth at milliKelvin does not increase when compared to samples at 3 K.With these samples, it was also possible to test a coupling regime between a NbN superconducting resonator and the samples, where the hybrid system creates an "avoided crossing" spectrum. The spectrum obtained showed characteristics of a weakly coupled system, where the magnonic system acts as a dissipation channel for the microwave photons, due to its currently high linewidth. These novel samples, together with the study of their losses and of the hybrid system, are a relevant step for future quantum magnonics experiments.

Keywords: Microwave engineering; Ferromagnetic resonance; MilliKelvin regime; Hybrid quantum circuits; Quantum magnonics

List of Figures

List of Tables

List of Acronyms

ADC Analog to Digital Converter

ADR Adiabatic Demagnetization Refrigerator

ALC Automatic Level Control

BVMSW Backward Volume Magnetostatic Wave

CPW Coplane Waveguide

DUT Device Under Test

FAA Ferric Ammonium Alum

FIB Focused Ion Beam

FMR Ferromagnetic Resonance

FVMSW Forward Volume Magnetostatic Wave

GGG Gallium Gadolinium Garnet

HEMT High Electron Mobility Transistor

HTS High Temperature Superconductor

IF Intermediate Frequency

IFBW Intermediate Frequency Bandwidth

LL Landau Lifshitz equation

LLG Landau Lifshitz Gilbert equation

LO Local Oscillator

LTS Low Temperature Superconductor

MBE Modified Bloch Equations

MSSW Magnetostatic Surface Spin Wave

MSW Magnetostatic Spin Wave

PCB Printed Circuit Board

PFIB Plasma Focused Ion Beam

PLL Phase Lock Loop

PT Pulse Tube

SS Stainless Steel

SW Spin Wave

TLS Two Level System

VCO Voltage Controlled Oscillator

VNA Vector Network Analyser

VSWR Voltage Standing Wave Ratio

YIG Yttrium Iron Garnet

Contents

7   Conclusions and Future Work   73

Appendices   75

Chapter 1

Introduction

The field of quantum technologies is a rapidly developing one. It relies on distinct and complex characteristics of quantum systems, such as superposition and quantum entanglement, to create unique devices with real-world applications in fields such as communications, sensing and computation. Different implementations of quantum devices can be achieved, but all rely on a single basic block called a qubit (quantum bit): a two-level quantum system that represents a unit of quantum information. Manipulation and probing of this quantum system is the fundamental working principle behind quantum sensors, computers and communications.

Superconducting quantum circuits are one way to implement such systems. These circuits are designed to simulate the behaviour of a two-level quantum system (with ground and excited state corresponding to the 0 and 1 state, respectively) with the help of a non-linear inductive and dissipationless circuit element called Josephson junction, as well as with other traditional reactive elements such as capacitors and linear inductors.

The interaction of these qubits with magnetic spin systems is worth its own field, called quantum magnonics [1]. The objective is precisely to study magnons (e.g. magnetostatic modes) interacting with a non-linear quantum system (qubit) and the resulting non-classical phenomena, such as strong and dispersive coupling regime between both. Majors applications of this field in future quantum technologies would be the transfer of quantum information between the two systems, as well as the possibility of sensing magnons on a quantum level [1]. Specifically, for the former, it would mean the creation of a quantum network of superconducting qubits, where the quantum state could be coherently transferred to a magnonic system and subsequently to a optical fiber network.

This work deals with one of the two fundamental systems in this field: magnetic

systems. To reach the desired regime of coupling, both systems need to be studied thoroughly, namely the losses in each system (which are measured by the linewidth of resonance curves) and the interaction of both systems with an essential third component, an intermediate microwave resonator. The magnetic material studied throughout this work is Yttrium Iron Garnet (YIG), known, to this date, for the lowest spin wave damping, in addition to being one of the most studied materials in the area [2–4].

Current experiments working with YIG hybrid quantum systems either use a three dimensional sphere with a microwave cavity (and a qubit) or a two dimensional thin film fabricated on a GGG substrate. Despite being *easier* to show properties of quantum magnonics with three dimensional systems, the 2D integration with superconducting quantum circuits is the desired application for these systems, particularly in future quantum computers and networks. However, it has been shown that the GGG substrate in YIG thin films increases significantly the spin wave damping at milliKelvin temperatures [5, 6], making it very tough to obtain strongly coupled hybrid circuits. At the same time, this substrate shows the lowest damping at room temperatures (due to very similar crystallographic lattices), so other substrates would only worsen the result. Room temperature results obtained are also shown in this thesis as a means of comparison, with both a YIG sphere and a thin film on a GGG substrate.

Here, early measurements on a novel type of YIG sample are shown. Being developed in the University of Glasgow [7], the samples were structured and placed on-chip with a Focused Ion Beam (FIB) technique, which does not require any substrate. In theory, this would mean that, at milliKelvin, these samples would have an extremely low spin damping, only being limited by their shape, dimensions and coupling to transmission line. It is also shown how these parameters influence the system behaviour.

This thesis is organized as follow: first two chapters are theoretical introductions to the topics discussed in this work (ch. 2 and 3), the following two chapters are concerned with the experimental setups used for both room and cryogenic temperatures (ch. 4 and 5). Afterwards, a compilation of the results obtained is presented (ch. 6) and the last chapter concludes this work (ch. 7).

Chapter 2

Microwave engineering

Microwave and radio frequency engineering has a fundamental difference to its low-frequency counterpart. In order to understand that difference, it is necessary to think of the electromagnetic physics behind electrons, where for higher frequencies, the wavelength of the signal becomes shorter such that the wave nature of the electrons need to be taken into consideration. At low frequencies, the wavelength is so long (@10MHz, $\lambda \sim$ 30m, Table 2.1) compared to the length of the electrical circuit that the voltage and current are well defined and are not dependent on the position where they are measured on a wire. On the other hand, at high-frequencies (@1GHz, $\lambda \sim$ 30cm) this starts to become a problem such that the signal amplitude and phase depend on the position on the wire. Therefore, to deal with such frequencies, special circuitry and components are required to maximize the effectiveness of transferring microwave power between them.

f (GHz)	λ (mm)	E (meV)
0.025	12×10^3	1.03×10^{-5}
1	300	4.1×10^{-3}
25	12	0.103
250	1.2	1.03

Table 2.1: Radiation properties for different frequencies in the microwave region of the electromagnetic spectrum. Wavelength λ (free space) and photon energy E values are approximations.

2.1 Fundamentals

2.1.1 Transmission lines

The fundamental component in every microwave circuit is the transmission line. It replaces the simple wires used at low frequencies and it is designed to effectively transmit high frequency signals with optimal power transfer and attenuation.

Transmission lines consist of at least two electrical conductors separated by a dielectric material with a characteristic impedance even in the ideal case of a lossless line (examples of implementations include coaxials, stripline, microstrip, coplanar, ...). This impedance always needs to be considered when designing and measuring microwave circuits since it is directly responsible for reflections of voltage and current travelling waves which will adversely affect the measurement and behaviour of the system.

The theory behind transmission lines is based on the distributed model, where infinitesimal lengths of the line are replaced by a lumped-element equivalent (i.e circuit characteristics are represented by discrete electronic components connected by ideal wiring) [8]. Each of these elements model a physical aspect of the line: R and L are the intrinsic resistance and self-inductance of the conductors, respectively, C is the capacitance due to having at least two conductors near each other and G is the conductance between the conductors which represents dielectric losses.
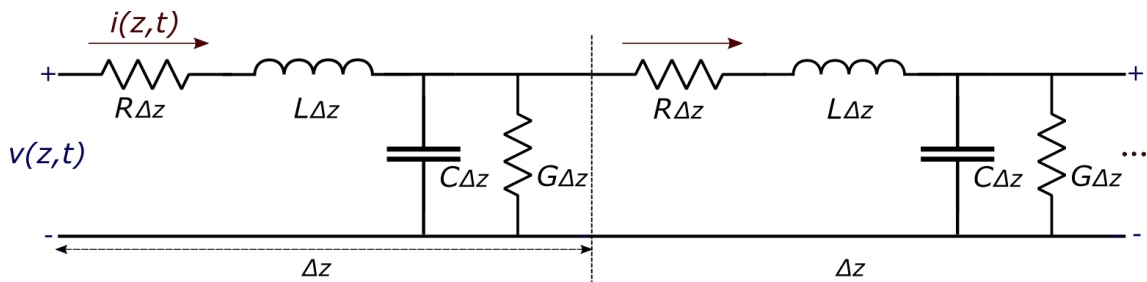
Figure 2.1: Lumped-element model of a transmission line. Losses in the line are represented by the series and shunt resistance (R, G), while electrical coupling of the conductors is represented by the series inductor and shunt capacitor (L, C).

Applying the Kirchhoff's voltage and current law to the lumped-element circuit (with $\Delta z \to 0$), the telegrapher's equations are obtained. These describe how the

voltage and current behave in a transmission line:

$$\frac{\partial v(z,t)}{\partial z} = -R\,i(z,t) - L\frac{\partial i(z,t)}{\partial t}, \tag{2.1}$$

$$\frac{\partial i(z,t)}{\partial z} = -G\,v(z,t) - C\frac{\partial v(z,t)}{\partial t} \tag{2.2}$$

where the $v(z,t)$ and $i(z,t)$ represent the voltage and current signals and the lumped element constants R, G, C, L are defined in Fig. 2.1.

The telegrapher's equations can be solved for standard steady-state sinusoidal signals (e.g. $v(z,t) = V(z)\,e^{j\omega t}$) in a finite-length transmission line and we get a wave equation which supports standing waves solutions during signal propagation:

$$\begin{cases} \frac{\partial V(z)}{\partial z} = -I(z)\,(R + j\omega L), \\ \frac{\partial I(z)}{\partial z} = -V(z)\,(G + j\omega C) \end{cases} \Rightarrow \begin{cases} \frac{\partial^2 V(z)}{\partial z^2} = \gamma^2\,V(z), \\ \frac{\partial^2 I(z)}{\partial z^2} = \gamma^2\,I(z) \end{cases} \tag{2.3}$$

The analytical solution to these equations is:

$$\begin{cases} V(z) = V_0^+\,e^{-\gamma z} + V_0^-\,e^{+\gamma z}, \\ I(z) = I_0^+\,e^{-\gamma z} + I_0^-\,e^{+\gamma z} \end{cases} \tag{2.4}$$

where, in each case, we have a wave travelling in the positive z direction ($e^{-\gamma z}$) and another one travelling in the negative z direction ($e^{+\gamma z}$) with a propagation constant given by γ. This complex constant is given by:

$$\gamma = \sqrt{(R + j\omega L)(G + j\omega C)} = \alpha + j\beta \tag{2.5}$$

with α and β the real and imaginary components of γ, related to a lossy and lossless propagation, respectively. The characteristic impedance of the line is then given by the ratio of the voltage and current waves travelling in the same direction $\left(\frac{V_0^+}{I_0^+}\right)$:

$$Z_0 = \sqrt{\frac{R + j\omega L}{G + j\omega C}} \tag{2.6}$$

In practice, most transmission lines are designed so that Z_0 is either 50 Ω or 75 Ω. It can be shown that for maximum power transfer, the optimal impedance is 30 Ω, while for minimum attenuation, the ideal impedance is 75 Ω. The standard for 50 Ω is a compromise between these two values.

As a result of travelling waves (eq. 2.4) in both directions, if the load impedance Z_L is not matched to the characteristic impedance of the line (i.e. they do not have the

same impedance), the sum of these waves will create standing waves in the line. In the extreme cases of terminating the line with a short or open circuit ($Z_0 = 0$ and $Z_0 = \infty$, respectively), voltage waves will fully reflect at these terminations and will add in-phase (open) or out-of-phase (short), creating standing nodes and valleys on the voltage and current signals.

To quantify the reflections on a transmission line (as well as on other microwave components), several coefficients can be defined to better describe the system such as the reflection coefficient Γ or the Voltage Standing Wave Ratio (VSWR):

$$
\begin{cases}
\Gamma = \frac{V_0^-}{V_0^+} = \frac{Z_L - Z_0}{Z_L + Z_0}, \\
\text{VSWR} = \frac{V_{max}}{V_{min}}
\end{cases}
\tag{2.7}
$$

The reflection coefficient is simply the ratio between the reflected and incident wave ($0 < |\Gamma| < 1$), while the VSWR is the ratio between the maximum and minimum value of the voltage signal ($1 < \text{VSWR} < \infty$). Another common coefficient defined from Γ is the return loss of the system and is simply given by $-20 \log |\Gamma|$ in dB.

2.1.2 Scattering parameters

To characterize systems using microwave instrumentation, one cannot use the standard voltage and current signals as a well defined measurement because the probe positioning would be troublesome, while its impedance would change the behaviour of the standing waves and result in a inaccurate measurement. Instead, measurements rely on the ability to directly detect the reflected and transmitted waves from the Device Under Test (DUT). From these signals, it is possible to completely characterize the DUT using the scattering parameters (or S-parameters) of the network.

A network is characterized by having n ports, each with two signals present (incident and reflected signal). In the case of a two-port DUT (Fig. 2.2), four signals will be present: a_1, b_1 are the incident and reflected voltage signals from port 1 and a_2, b_2 the same for port 2. From these, it is possible to defined the scattering parameters of the system (n^2 parameters for a n port network):

$$
\begin{aligned}
S_{11} &= \frac{\text{Reflected signal seen from port 1}}{\text{Incident signal from port 1}} = \frac{b_1}{a_1}, \\
S_{22} &= \frac{\text{Reflected signal seen from port 2}}{\text{Incident signal from port 2}} = \frac{b_2}{a_2},
\end{aligned}
$$
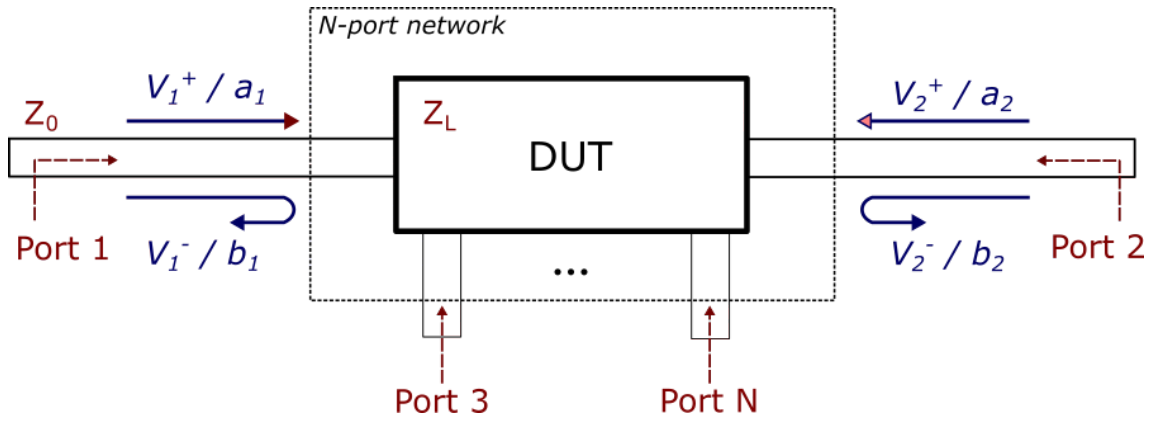
Figure 2.2: Direct characterization of n-port DUT using reflected and transmitted microwave signals.

$$S_{21} = \frac{\text{Transmitted signal reaching port 2}}{\text{Incident signal from port 1}} = \frac{b_2}{a_1},$$
$$S_{12} = \frac{\text{Transmitted signal reaching port 1}}{\text{Incident signal from port 2}} = \frac{b_1}{a_2}$$

In practice, to obtain all parameters, one has to do n measurements since the microwave power has to be switched from port 1 to port n, while, at the same time, all other ports are terminated with a matched load (for instance, to measure S_{11}, port 2 has to be terminated with a Z_0 load, while power is being transmitted from port 1). Generalizing for n port network, each element of the scattering matrix is defined as a ratio between reflected and transmitted waves:

$$S_{ij} = \left. \frac{V_i^-}{V_j^+} \right|_{V_k^+ = 0 \text{ for } k \neq j} \tag{2.8}$$

using the same notation as in equation 2.4 and with the subscript defined as the port number.

It is also important to notice that S-parameters are complex quantities and, as such, to fully characterize the network, both amplitude and phase of the parameters are necessary (as will be discussed in the next section, this is the difference between vector and scalar network analysis). However, it is common to redefine the amplitude of some of the scattering parameters and transform them to a logarithmic scale. Considering the DUT stimulated from port 1, it is possible to define the following parameters of the DUT:

$$\text{Gain/Insertion loss (dB)} = \pm 20 \log |S_{21}|,$$
$$\text{Isolation (dB)} = -20 \log |S_{12}|,$$

$$\text{Input Return loss (dB)} = -20 \log |S_{11}|,$$
$$\text{Output Return loss (dB)} = -20 \log |S_{22}|$$

2.2 Vector Network Analysis

Network analysers are instruments used to characterize a microwave network by determining its response to a well-calibrated stimulus coming from the instrument. A Vector Network Analyser (VNA) is an example of such instrument and it is the most commonly used one in microwave instrumentation due to its ability to fully determine the scattering parameters (both amplitude and phase). While the complexity of the system increases to be able to measure phases, it is also one of its strengths, since with the phase information it is possible to implement an elaborated error correction algorithm (e.g. to compensate for the requirement to exactly match the unstimulated ports and also due to inevitable electronic noise) and to easily Fourier transform into the time domain [10].

Since it is the most important instrument when it comes to testing and measuring devices in this frequency range, this section is dedicated to describe how VNAs are able to very precisely determine S-parameters, as well being able to do a wide range of linear, non-linear and time-domain measurements.

2.2.1 Principles of operation

VNAs are a stimulus/response system, meaning that the microwave signal is generated and detected by the instrument itself. The following steps are essential to the operation of any VNA:

- A high frequency signal is generated by the synthesizer and provides the stimulus for the DUT. This signal is controlled with specialized circuitry to provide stable frequency and phase, with Phase Lock Loop (PLL) circuits, and stable power, with Automatic Level Control (ALC) circuits. The signal generated is fed into a microwave switch block which selects the correct port to measure.

- Next, the signal is separated using a directional coupler which splits the signal into a test (T) and reference (R) signal. The test signal is fed into the DUT (from the port where the signal is active) and the resulting reflected signal goes through a second directional coupler which couples it to a receiver. The reference signal is coupled to the same receiver through the first coupler. Other ports, which are not being stimulated by the synthesized signal, receive the

transmitted signal from the DUT and this signal is coupled to the receiver with a directional coupler.

- On each receiver, the microwave signal is down-converted to an intermediate frequency (IF) using an heterodyne scheme, so it can be fed into an Analog-to-Digital converter (ADC). After being digitized, the signals are processed and analysed by the processing unit (on-board computer).

It is possible to divide this operation cycle into three blocks: frequency generation, signal separation and receiver/signal processing:

Microwave frequency generation

The stimulus for the DUT, called the source signal, is synthesized inside the VNA using two oscillators: a tunable oscillator (e.g. voltage controlled oscillators (VCO) or tunable YIG oscillators) controlled by a PLL circuit to achieve high frequency stability and purity and a fixed frequency oscillator (e.g. temperature compensated oscillators) which acts as a precise and stable reference to synthesize signals such as the source and Local Oscillator (LO).

Both signals are the base for the PLL circuit which locks their phase and frequency together by comparing the phase output of the VCO with the fixed frequency oscillator in a feedback loop scheme and adjusting the VCO accordingly. It is also in the PLL circuit that the VCO can be tuned to any frequency within its range, since the VNA usually operates in a continuous frequency sweep mode where, for every cycle of the measurement, the frequency is changed to determine the spectrum of the DUT.

To control the output power of the source, the ALC works by implementing a feedback loop in which the output signal from the PLL (known power) is adjusted to a certain output level within the range of the instrument (typical values between -10 and 10 dBm). This circuitry allows the VNA to operate in a power sweep mode, similar to frequency sweeping.

For higher frequencies than the oscillators can provide, VNAs use frequency multiplier components which generate harmonics of the input signal frequency. It works by using a non-linear element such as a diode/transistor which, by definition, generate harmonics whose magnitude depend on the input power. By selecting and conditioning a specific harmonic, the desired output frequency can be obtained with a conversion efficiency which depends on the architecture of the multiplier (up to 100% theoretically).

Signal separation

Since a VNA works by calculating ratios of incident and reflected voltage signals, this block is essential to separate them in each port of the instrument. At the heart of this separation is a component called a directional coupler which offers directionality to the system, rejecting waves which travel opposite to a specific direction.

Directional couplers are four-port devices in which the signal travels through port 1 to port 2 undisturbed while it also couples to a third port (the forth port is isolated and internally matched, effectively making it a three-port device). When the direction is reversed, with signal from port 2 to 1, there is no longer any coupling to the third port. In practice, the isolation is not perfect and this reverse signal leaks to the main signal through the coupling port. The directivity (in dB) parameter measures how well the coupler can separate the desired and unwanted signal and it is one of the most relevant source of errors in an uncalibrated S-parameter measurement [9].

At least two couplers per port are necessary to build this block: a port coupler and the reference coupler. The reference coupler is used to split the source signal so that the instrument has a portion of the signal to use as a reference when calculating the S-parameters, while the rest of the signal continues to the port coupler. This coupler is used to separate the incident (a_i) and reflected signal (b_i) from the DUT by setting the coupled port to only accept the latter. By using this setup for each port, all necessary signals are determined by the instrument and the S-parameters can be calculated accurately after calibration.

Receiver module and Processing

Since the phase of the signals is as important as the amplitude, VNAs use a heterodyne tuned receiver to translate the microwave frequency signal into a lower frequency that can be digitized using an ADC, without losing any information about the original signal.

Frequency mixers are three-port devices that convert signal frequencies using a nonlinear element such as a diode or transistor, much like frequency multipliers. The output of a (double balanced) mixer is a signal with a frequency equal to the sum and difference of the two inputs ($f_{out} = f_{input1} \pm f_{input2}$), therefore, it is essential to filter it to select the desired sideband. The bandwidth of this filter can be modified by the instrument using the Intermediate Frequency Bandwidth (IFBW) parameter. Low IFBW (e.g. 100 Hz) means the IF output signal has a very narrow band which rejects all received broadband noise from the microwave signal, increasing the

dynamic range and harmonics rejection of the instrument.

The IF signal is additionally conditioned (amplifiers, filters) to the characteristics of the ADCs and it is there digitized with high resolution. The resulting signal is processed in a Digital Signal Processing (DSP) module followed by analysis on the main processing unit. This analysis includes a twelve-term (for 2-port system) error correction model which accounts for six major systematic errors (directivity, crosstalk, source and load match, reflection and transmission tracking) in both forward and reverse directions [9]. The correction is done using known standards for short, open, through and load measurements.

2.2.2   System block diagram

To sum up, Fig. 2.3 shows a general block diagram of an two-port VNA with all the mentioned blocks highlighted.
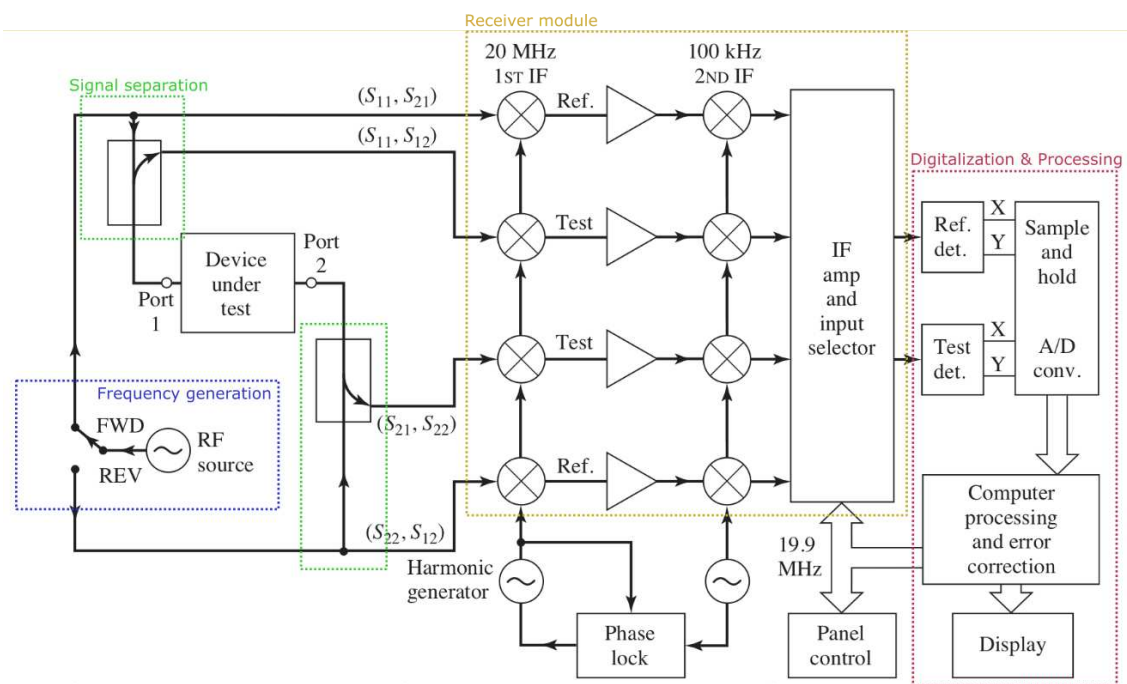
Figure 2.3: System block diagram of a generic Vector Network Analyser (VNA) with main functional blocks highlighted. The signal flows from the microwave frequency generation to the separation block, resulting in test and reference signals which are down-converted to an intermediate frequency (IF) in the receiver module to be digitized and processed. Adapted from [8]

2.3 Microwave resonators

Superconducting resonator circuits are essential for a range of applications from quantum computers (coupled to qubits for control and measurement) to photon detectors and classical narrowband microwave filters. When cooled down below the critical temperature T_c, the resonator enters a superconducting state and high quality factors Q can be obtained which translates into extremely low dissipation of energy in every cycle of resonance.

These resonators usually have a Coplanar Waveguide (CPW) design (Fig. 2.4), consisting of three superconducting strip wires (each separated by a small gap w_g) on the same side of the substrate, with the center strip (width w_c) being the signal conductor and the other two ground planes. This planar geometry is essential since it is easily integrated and fabricated with other on-chip quantum devices (such as superconducting qubits), while, on the other hand, only one layer of superconductor film deposition is necessary in this structure. It is also possible to design planar lumped element superconducting resonators, where the capacitors and inductors consist of meanders and gaps within the transmission line.
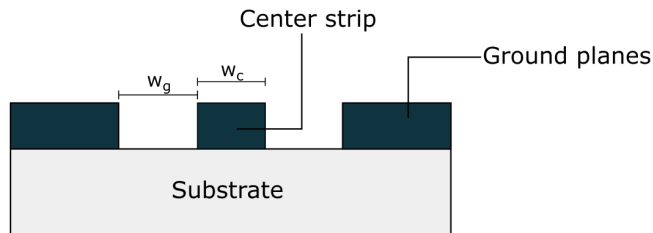
Figure 2.4: Cross section of a CPW thin film transmission line. The conductors (dark) are made of superconducting materials such as NbTi or Al, while the substrate (light) is usually sapphire (Al_2O_3), silica (SiO_2) or silicon (Si).

Superconducting CPW resonators are an extension of the traditional microwave transmission line resonators, therefore the base theory of operation of such structures can be understood from classical microwave theory. Resonators are traditionally built using lumped-element capacitors (C), inductors (L) and resistors (R) in well-known RLC lossy resonant circuits, however, as it was seen in chapter 2.1, transmission lines are the fundamental component at high-frequencies and it is shown that, depending on the length and terminations, they also form resonating circuits.

2.3.1 Transmission line resonators

Assuming the lossy model of the transmission line (eq. 2.6), if we consider a terminated line with a load impedance of Z_L, the input impedance of the system is given by the equation [8]:

$$Z_{in} = Z_0 \frac{Z_L + Z_0 \tanh \gamma l}{Z_0 + Z_L \tanh \gamma l} \tag{2.9}$$

where Z_0 is the characteristic impedance of the line and γ the complex propagation constant.

Common configurations include the half ($\lambda/2$) and quarter ($\lambda/4$) wavelength resonators, which refer to the length of the transmission line l at the desired frequency of resonance, ω_0. These lengths of line can be either open or short circuited to form a resonator, however, it is common in superconducting quantum circuits to have them open and capacitively (and weakly) coupled to the feedline, both at the input and output ports. A open circuit version of the resonator ($Z_L = \infty$) has a input impedance of:

$$Z_{in} = \frac{Z_0}{\tanh (\alpha + j\beta)l} = Z_0 \frac{1 + j \tanh (\alpha l) \tan (\beta l)}{\tanh (\alpha l) + j \tan (\beta l)} \tag{2.10}$$

where the sum property of the hyperbolic tangent was used. The expression can be simplified considering the loss in the line is low enough so that $\tanh \alpha l \approx \alpha l$ and that the CPW design supports quasi-TEM modes, such that the imaginary component β of the propagation constant can be written as $\beta = \omega l / v_p$, where v_p is the phase velocity of the waves in the transmission line. To show the resonant properties of this configuration, lets consider the behaviour around the resonant frequency, $\omega \rightarrow \omega_0 + \Delta\omega$, of an half-wavelength resonator with $l = \lambda/2 = \pi v_p / \omega_0$:

$$\tan \beta l = \tan \left(\frac{\omega_0 l}{v_p} + \frac{\Delta\omega l}{v_p} \right) = \tan \left(\pi + \frac{\Delta\omega \pi}{\omega_0} \right) \overset{\Delta\omega \ll \omega_0}{\approx} \frac{\Delta\omega \pi}{\omega_0} \tag{2.11}$$

Therefore, the final input impedance is given by:

$$Z_{in,\lambda/2} = Z_0 \frac{1 + j\alpha l \left(\Delta\omega \pi / \omega_0 \right)}{\alpha l + j(\Delta\omega \pi / \omega_0)} \overset{\Delta\omega/\omega_0 \ll 1}{\approx} \frac{1}{\alpha l / Z_0 + j(\Delta\omega \pi / \omega_0)/Z_0} \tag{2.12}$$

It can be shown that this formula is of the same form as the input impedance of a parallel RLC resonator [8], with equivalent R,L,C constants, therefore showing that the transmission line circuit also has resonance properties. Despite only using the fundamental resonant frequency in this section, CPW and all resonators have higher harmonic modes of resonance due to the boundary condition at the short/open end

(for instance, frequencies that are a multiple of the fundamental one also exhibit resonance properties), as well as possible coupling to the surroundings (box holder, package, ...).

Another important property of resonators is called the quality factor Q and it is defined as 2π times the average electromagnetic energy stored in the resonator divided by the energy loss per unit of time. For parallel RLC and half-wavelength open CPW resonators, Q is written as:

$$Q = \omega_0 RC = \frac{\beta}{2\alpha} \tag{2.13}$$

where $R = Z_0/(\alpha l)$ and $C = \pi/(2\omega_0 Z_0)$ are the equivalent RLC constants for the CPW resonator. This result is also known as the internal Q_i factor because it does not take into consideration the effects of any coupling to external loads and, as such, relates to the internal losses of the resonator. On the other hand, the coupling or external Q_c factor is associated with coupling losses to the feedline readout circuit, which can be either inductive or capacitive. The total or loaded quality factor Q_l is related to these two by the expression:

$$\frac{1}{Q_l} = \frac{1}{Q_i} + \frac{1}{\text{Re}\{Q_c\}} \tag{2.14}$$

using a model where the coupling factor is a complex number which accounts for impedance mismatches, as mentioned in Ref. [11].

Regarding the coupling quality, it is possible to distinguish three regimes of operation: when the losses to the external circuit are greater than the internal losses ($Q_i > \text{Re}\{Q_c\}$), the resonator is overcoupled to the feedline, while when the internal losses are greater, the resonator is undercoupled ($Q_i < \text{Re}\{Q_c\}$). If the external and internal losses are equal, there is a critical couple of the resonator to the feedline and this situation translates to the maximum power transfer in the system.

2.3.2 Superconducting characteristics

The goal of using superconductors to form microwave resonators is to take advantage of their intrinsic low loss microwave conduction to achieve high quality factors. When a superconductor crosses the critical temperature T_c, the electrical conductivity $\sigma(\omega)$ changes drastically since Cooper pairs become the dominant charge carriers. This translates into the well-known zero DC resistivity, while at higher frequencies (below the superconducting band gap frequency) the complex conductivity ($\sigma(\omega) = \sigma_1(\omega) - j\sigma_2(\omega)$) is given by the Mattis-Bardeen equations [12]. It can be shown that

the dissipative component of the conductivity (real part) disappears as temperatures reach absolute zero, whereas the reactive component (imaginary) is always present, even at $T = 0$ K, which is associated with the inertia of Cooper pairs and is, indirectly[1], responsible for the low AC dissipation.

For a superconducting resonator, the internal quality factor Q_i depends on its surface impedance $Z_s = R_s + jX_s$ which is related to the complex conductivity as in Ref. [13]. Like $\sigma(\omega)$, the reactive component is generally much greater than the resistive one at $T \ll T_c$ so that large values of the surface impedance quality factor $Q_s = X_s/R_s$ can be achieved. Q_s and Q_i are related to one another by a proportionality constant which depends on the type of the resonator (cavity or microresonator).

For CPW and microstrip resonators, the characteristic impedance is given by equation 2.6, where it is seen that, even for a perfectly conducting line (R, $G = 0$), the impedance is a function of the inductance and capacitance of the system. The effect of using a superconductor is seen as an increase in this inductance due to the additional kinetic inductance component of the superconductor's surface impedance. In this case, the internal quality factor is given by:

$$Q_i = \alpha_{sc}^{-1} Q_s \tag{2.15}$$

where α_{sc} is the kinetic inductance fraction of the total line inductance (≤ 1).

In theory, superconducting resonators should have quality factors tending to infinity as temperature reaches absolute zero, as predicted by theory (black curve Fig.2.5). In practice, the coupling to the feedline is usually the limiting factor (red curve Fig.2.5). Nonetheless, even after overcoming the overcoupling problem, there are two extra mechanisms which inhibit this ideal behaviour and are not related to the superconductor itself, but rather to fabrication and design considerations [14]. The first loss mechanism is related to radiation loss to free space, as well as to the input line, and it can be managed by adjusting the coupling quality factor, creating lithographic patterns and features on CPW that help to prevent it or implementing a lumped-element resonator [13].

---

[1]Superconducting electrons generate internal AC fields which interact with few normal electrons, causing dissipation.
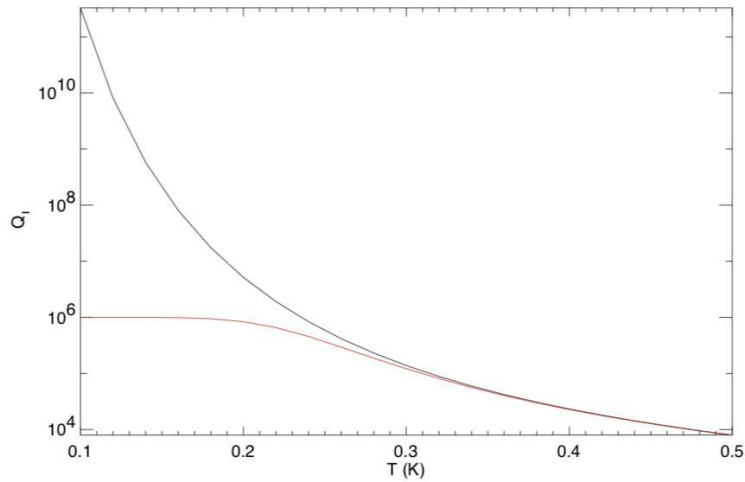
Figure 2.5: Quality factor of an ideal (black) and a coupled-limited (red) superconducting resonator. Taken from Ref. [15]

The second and most limiting mechanism of dissipation is related to the existence of Two-Level Systems (TLS) in the bulk dielectric material and on very thin layers at the interfaces between superconductor/dielectric and superconductor/air [16]. These systems resonantly absorb microwave power at frequencies near the resonator's frequency, acting as an unwanted dissipation channel. This mechanism is behind dielectric loss which is quantified by the loss tangent of the material ($\tan\delta$) and represents the fraction of electromagnetic energy that is dissipated at the dielectric.

Ways to reduce the loss from TLS have been proposed like utilizing superconductors with low surface oxides [17], widening the gaps for CPW resonators, applying high microwave power signals or even decreasing the frequency [14]. Despite these solutions, most of them are not suitable for quantum regime applications and imply a trade-off when designing resonators. For instance, increasing the widths of CPW's center conductor decreases losses from TLS defects due to the smaller fraction of the eletric field that interacts with them, but the radiation loss gets worse at the same time. Applying high power signals also decreases loss from TLS, but the resonator cannot operate at the single photon quantum regime of interest.

Chapter 3

Ferromagnetic Resonance (FMR)

Ferromagnetic resonance is one of the most important techniques of modern microwave spectroscopy and it is defined as the resonant absorption of energy from high-frequency electromagnetic fields in magnetically ordered materials [18]. The use of microwave radiation and the small energy of their photons ($\sim$ 0.1-1 meV, Table 2.1) is the reason this technique is so powerful when it comes to probing very fine details of the atomic properties of many materials (such as atomic structures and anisotropies), as well as the dynamics of the magnetization.

In typical FMR experiments, there are two different fields applied to the ferromagnetic sample: a static magnetic field H_0 and a weak high frequency (h.f.) electromagnetic field $h_0(t)$ applied at a right angle to H_0. In early setups, the h.f. field was usually kept at a specific frequency while the external magnetic field was swept across a range of values. However, recently, the opposite has become more common: sweep a wide frequency range and keep the external magnetic field constant. This technique is called broadband FMR or VNA-FMR and it is used to study the frequency dependence of damping factors and dynamics [19–22]. As we will see later in this work, it is also possible to do a two dimensional sweep of frequency and current simultaneously, which results in a detailed characterization of FMR. Other techniques to probe the magnetization dynamics include pulsed inductive microwave magnetometry and the time resolved magneto-optic Kerr effect.

3.1 Origin of ferromagnetism

The Bohr-van-Leeuwen theorem states that, applying classical mechanics in thermal equilibrium, the average magnetization of a sample will be always equal to zero,

therefore not allowing the existence of ferromagnetism [23]. The only explanation for spontaneous magnetism can only come from a purely quantum mechanical theory in which this magnetic ordering is a result of the strong exchange interactions (of electrostatic nature) between the localized spins in the lattice. Therefore, ferromagnetism can be defined as a collective ordering of the spin magnetic moments of the inner shell electrons of atoms due to the strong exchange interactions between them, without any applied external fields.

Ferromagnetism, like other phenomena in solid state physics such as superconductivity, is a result of symmetry breaking below a specific temperature which translates to a spontaneous ordering of the system [24]. A broken rotational symmetry in ferromagnetism corresponds to a phase transition from a paramagnet to a ferromagnet when the material cools down from the Curie temperature. Broken symmetries have common properties such as the existence of an order parameter that is zero above the critical temperature (magnetization), rigidity and defects (domains).

One of the consequences of the broken symmetry is the creation of domains in the material. In each domain, all the spins are aligned in the same direction, which can be treated classically as a single macro-spin. Some ferromagnets in the ground state have an effective null magnetization due to the randomly oriented domains which cancel out, while some have a well defined magnetization. However, once an external magnetic field is applied, all the spins will tend to orient in its direction. Eventually, as the applied field becomes stronger, all the spins and domains will be aligned in the same direction and a saturation value for the magnetization of the sample will be reached.

3.2 Magnetization dynamics

3.2.1 Larmor precession

When a ferromagnetic sample is magnetized by a strong external field, a single magnetic domain is created and the resulting magnetization vector $\mathbf{M}$ is given by the vector sum of the magnetic moment $\boldsymbol{\mu}$ of each electron per unit volume (if the field is strong enough, the magnetization reaches a saturation value which is dependant on the sample).

To find the resonance condition, it is essential to describe the dynamics of the magnetization vector. Classically, the magnetic and angular momentum are related by the gyromagnetic (also magneto-mechanical) ratio γ and the same happens with

the spin of the electron. The magnetic moment $\boldsymbol{\mu}$ and the spin $\mathbf{s}$ are related by the same ratio:

$$\boldsymbol{\mu} = -\gamma_e \, \boldsymbol{s} \tag{3.1}$$

Particularly, the electron gyromagnetic ratio has a value of $|\gamma_e/2\pi| \approx 28.02495$ GHz/T. Since we are dealing with strongly interacting electrons in magnetic systems, γ will refer to the electron ratio throughout the remaining of this work. The gyromagnetic ratio is also is related to another constant which is the spectroscopic splitting factor g by the expression $\gamma = -g \frac{e}{2mc}$.

Taking the derivative on both sides of eq. 3.1 and knowing the expression for the torque on a magnetic moment, the first equation obtained to express the dynamics of $\mathbf{M}$ in a magnetic field $\mathbf{H}$ is:

$$\frac{d\mathbf{M}}{dt} = -\gamma \left(\mathbf{M} \times \mathbf{H} \right) \tag{3.2}$$

This equation is known to describe the lossless precession of the magnetization vector around the external magnetic field H_0 and the frequency of this motion is given by the famous Larmor frequency:

$$\omega_0 = \gamma \, H_0 \tag{3.3}$$

As a first, very crude approximation, this result only works for a few special cases of FMR (namely, spheres in uniform external fields). However, by substituting the magnetic field in the expression by an effective field H_i, a significant improvement can be done to the resonance condition which better matches experimental results.

3.2.2 Internal magnetic field H_i

There are different mechanisms which contribute to the effective field that interacts with the system of spins [18]. To start, the shape of the sample is directly related to the so-called demagnetizing fields $\mathbf{H}_d$ which are the fields created by the magnetization itself and, therefore, affect the way the whole sample reacts to the external field. Assuming a homogeneous magnetization on the whole sample (this assumption is valid when there is a strong external magnetic field that creates one single domain of magnetization on the sample), the internal field $\mathbf{H}$ is given by:

$$\mathbf{H} = \mathbf{H}_0 + \mathbf{H}_d \tag{3.4}$$

where $\mathbf{H}_0$ is the applied external field with the static component $H_0\hat{\mathbf{k}}$ and h.f component $\mathbf{h}(t) = h_x(t)\hat{\mathbf{i}} + h_y(t)\hat{\mathbf{j}} \ll H_0$ and $\mathbf{H}_d = -\mathcal{N}\mathbf{M}$, with demagnetization tensor

$\mathcal{N} \equiv N_{ij}$ $(i = x,y,z)$ whose three diagonal terms N_{ii} are the demagnetization factors for each axis. The result of the applied field is seen in the magnetization vector which can be written as $\mathbf{M} = M_s\hat{\mathbf{k}} + \mathbf{m}(t)$, with $\mathbf{m}(t)$ being the small precessing component of the magnetization, perpendicular to the static field, and assuming this field is strong enough to saturate the magnetization component in the $\hat{\mathbf{k}}$ direction.

Substituting the new effective H field and the magnetization in equation 3.2, we obtain a system of three equations describing the evolution of magnetization with time:

$$-\frac{1}{\gamma}\frac{dm_x}{dt} = m_y(t)[H_0 - N_z M_s(t)] - M_s(t)[h_y(t) - N_y m_y(t)], \qquad (3.5)$$

$$-\frac{1}{\gamma}\frac{dm_y}{dt} = -m_x(t)[H_0 - N_z M_s(t)] + M_s(t)[h_x(t) - N_x m_x(t)], \qquad (3.6)$$

$$\frac{dM_s}{dt} \simeq 0 \qquad (3.7)$$

Solving the coupled differential equations with a time dependence $e^{j\omega t}$ of the transverse magnetization $\mathbf{m}(t)$ and h.f. field $\mathbf{h}(t)$, the resonance condition is obtained:

$$\omega_0 = \gamma \sqrt{[H_0 + (N_x - N_z)M_z][H_0 + (N_y - N_z)M_z]} \qquad (3.8)$$

This formula shows the dependence of the resonance frequency on the shape of the sample which is related to the demagnetizing factors and also on the saturation magnetization M_z (which depends on the material and temperature). A special case of this formula is a spherical sample ($N_{x,y,z} = 1/3$) with a resonance frequency of $\omega_0 = \gamma H_0$ (eq. 3.3). Another important case is the Kittel formula for thin films ($N_{x/y} = 1$, $N_{y/x}$, $N_z = 0$) with in-plane direction of H_0:

$$\omega_0 = \gamma \sqrt{H_0 (H_0 + M_s)} \qquad (3.9)$$

While for a out-of-plane saturation magnetization ($N_z = 1, N_{x,y} = 0$):

$$\omega_0 = \gamma (H_0 - M_s) \qquad (3.10)$$

Despite being true only for the case of an ellipsoidal sample, this result was able to correctly predict some results regarding the shape of the sample in FMR experiments [25].

3.2.2.1 Anisotropy

Anisotropies present in magnetic samples also change the effective magnetic field felt by the spins in the material. There are two types of anisotropies that will be studied and analysed in this work: *magnetocrystalline anisotropies* are an intrinsic property of the material, specifically of its crystal lattice, which makes it easier to magnetize the sample in one particular direction (easy axis) compared to others. This characteristic is a result of atomic structure, particularly spin-orbit interactions [24]. On the other hand, *shape anisotropies* are related to the different demagnetization factors that exist on non-spherical samples which leads to direction dependant demagnetization fields and to the creation of an easy axis. This type of anisotropy is a direct result of long range dipolar interactions which makes it possible to study using a classical theory, as seen in the previous section.

For the case of magnetocrystalline anisotropies, and depending on the crystal structure of the sample, different corrections to equation 3.8 can be made. For a crystal with cubic symmetry, the free energy of the crystal magnetic anisotropy is given by [18]:

$$F_{ani} = K_1 \left(\alpha_1^2 \alpha_2^2 + \alpha_2^2 \alpha_3^2 + \alpha_3^2 \alpha_1^2 \right) + K_2 \left(\alpha_1^2 \alpha_2^2 \alpha_3^2 \right) + ... \tag{3.11}$$

where α_i are the direction cosines between the saturation magnetization and the edges of the cube structure and K_1, K_2 are the first and second order magnetic anisotropy constants, respectively. In particular, this expression can be simplified for a crystal with uniaxial symmetry:

$$F_{ani} = K_1 \sin^2 \theta + K_2 \sin^4 \theta + ... \tag{3.12}$$

where θ is the angle between the applied magnetic field and the easy axis of the crystal. The derivative of the free energy in respect to the angle θ is the torque produced by this anisotropy. Therefore, it is similar to an extra internal field which adds up to the previous effective field:

$$H_{ani} = \frac{2|K_1|}{M_s} \tag{3.13}$$

where M_s is the saturation magnetization and K_1 the same constant as before. For a sphere with this symmetry, the addition of this anisotropy field would result in a new resonance condition:

$$\omega_0 = \gamma \left(H_0 + H_{ani} \right) \tag{3.14}$$

This result is a very particular case with the goal to demonstrate that the resonance condition changes due to anisotropies. Overall, the exact solution is both dependant

on the crystal symmetry, the shape of the sample and the direction of the applied field and, therefore, of the saturation magnetization [18].

3.2.2.2 Domain structure

Another important characteristic of ferromagnetic materials is the domain structure. If the external static field is not strong enough to create a single domain, the sample will have smaller domains which, in turn, will have a smaller free energy than the single domain structure. At the domain walls, two different magnetization vectors can be defined $\mathbf{M}_1$, $\mathbf{M}_2$ which have different orientations (due to the multi domain structure) and depending on the direction of the applied h.f. field, these vectors can either precess in phase or counter-phase, altering the resonance condition for the sample [18]. This phenomenon is specially important when dealing with magnetic fields not strong enough to create a single domain, so each domain contributes differently to the resonance effect.

3.2.2.3 Anti-ferromagnetic materials

So far it has been assumed the material is ferromagnetic, however, anti-ferromagnetic and ferrimagnetic materials also exhibit resonance phenomena. The total magnetization of the sample will be given by the vector sum of each magnetization $\mathbf{M}_i$ (which can be parallel or anti-parallel to each other). Applying the magnetization dynamics equation 3.2 to each $\mathbf{M}_i$ with an effective field $\mathbf{H}_i$, a system of equations now has to be solved. As an example for a crystal with two sub-lattices $\mathbf{M}_{1,2}$ anti-parallel to each other, the solutions to the system of equations will result in two different resonance frequencies: one low frequency precession which is similar to a ferromagnetic resonance ($\omega_1 = \gamma_{\text{eff}} H_0$) and a high frequency oscillation which is determined by the molecular field of the crystal [18].

3.2.3 Landau-Lifshitz equation

Until now, it has been assumed that the precession motion is lossless, meaning that it has no possible way of dissipating energy and stopping. This is the cause of the absence of a line width in the discussion above. Therefore, to get the correct shape of the absorption line, Landau and Lifshitz [26] added a relaxation term to equation 3.2, obtaining the Landau-Lifshitz (LL) equation:

$$\frac{d\mathbf{M}}{dt} = -\gamma \left(\mathbf{M} \times \mathbf{H}_{\text{eff}} \right) - \alpha \frac{\gamma}{M} [\mathbf{M} \times (\mathbf{M} \times \mathbf{H}_{\text{eff}})] \tag{3.15}$$

with α being the non-dimensional damping factor. Classically, this relaxation term makes the precession motion have a finite duration and it eventually ends with the magnetization vector being aligned with the external static field in an equilibrium position (Fig. 3.1).
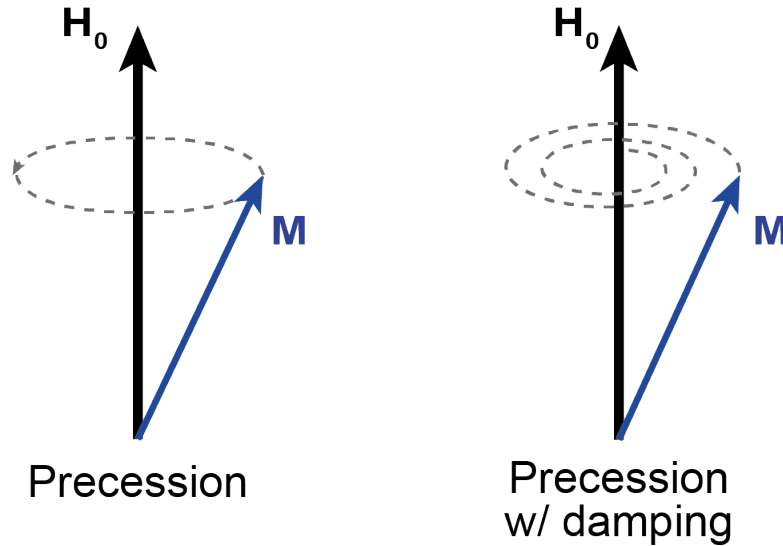
Figure 3.1: Precession motion of the magnetization vector in an external field. On the left, the lossless motion given by equation 3.2. On the right, the addition of the relaxation term as in equation 3.15 leads to damping.

With this term, the linewidth can be explained as the effect of the relaxation time on the resonance frequency. The relaxation effect may have different origins depending on the sample, such as a multi-domain structure, structural defects or coupling of the magnetization to spin waves, eddy currents and lattice vibrations [27].

The LL equation was the first equation to solve the problem of the line width, however, there were some problems encountered, specially when the damping was large. In an attempt to solve this problem, Gilbert [27] replaced the relaxation term with a new one:

$$\frac{d\mathbf{M}}{dt} = \gamma' \left(\mathbf{M} \times \mathbf{H}_{\text{eff}}\right) - \frac{\alpha}{M} \left(\mathbf{M} \times \frac{d\mathbf{M}}{dt}\right) \tag{3.16}$$

where $\gamma' = \gamma(1 + \alpha^2)$. This equation is called the Landau–Lifshitz–Gilbert (LLG) equation and it is mathematically equivalent to LL equation, despite small variations of the defined parameters α and γ. In the case of FMR experiments, the damping factor α is small enough that the LL equation can be applied without introducing a significant error.

Another problem with LL equation was the fact that the damping factor was treated as a scalar parameter, meaning that the relaxation effect was isotropic. The solution

was given by Baryakhtar [28], where the equation of motion was written as:

$$\frac{1}{\gamma}\frac{d\mathbf{M}}{dt} = -(\mathbf{M} \times \mathbf{H}_{\text{eff}}) - \hat{\alpha}\,\mathbf{H}_{\text{eff}} \tag{3.17}$$

Here, $\hat{\alpha} = \alpha_{ij}$ is a relaxation tensor which takes into account the anisotropy of magnetic crystal structures.

The last detail missing from the LL equation was the thermal effect on the magnetization dynamic. To this effect, the Landau-Lifshitz-Bloch (LLB) equation describes magnetization at finite temperatures for a ferromagnet [29]:

$$\frac{1}{\gamma}\frac{d\mathbf{M}}{dt} = -(\mathbf{M} \times \mathbf{H}_{\text{eff}}) + \alpha_{\parallel}\frac{(\mathbf{M} \cdot \mathbf{H}_{\text{eff}})\mathbf{M}}{M^2} - \alpha_{\perp}\frac{[\mathbf{M} \times (\mathbf{M} \times \mathbf{H}_{\text{eff}})]}{M^2} \tag{3.18}$$

where $\alpha_{\parallel}$ and $\alpha_{\perp}$ are dimensionless longitudinal and transverse damping parameters that are a function of the temperature T.

3.2.4   Modified Bloch equation

A distinct approach to the problem of understanding the magnetization dynamics are the Modified Bloch Equations (MBE) [30]. Bloch proposed the following equation to describe the magnetization dynamics in nuclear magnetic resonance experiments [31]:

$$\frac{d\mathbf{M}}{dt} = -\gamma\,(\mathbf{M} \times \mathbf{H}_{\text{eff}}) - \frac{M_x}{T_2}\mathbf{i} - \frac{M_y}{T_2}\mathbf{j} - \frac{M_z - M_0}{T_1}\mathbf{k} \tag{3.19}$$

where T_1 and T_2 are the longitudinal and transverse relaxation times and $\mathbf{M} = (M_x, M_y, M_z)$. This equation was not fit for the ferromagnetic resonance effect, specially because Bloch's equation was mainly used in strong alternating fields which is exactly the opposite of FMR procedures. A correction to the MBE was given by Torrey, Olds, Codrington [32] to better describe the FMR effect:

$$\frac{d\mathbf{M}}{dt} = -\gamma\,(\mathbf{M} \times \mathbf{H}_{\text{eff}}) - \left(\frac{1}{T_1} - \frac{1}{T_2}\right)\left(\frac{(\mathbf{M} \cdot \mathbf{H}_{\text{eff}})\,\mathbf{H}_{\text{eff}}}{H^2}\right) + \chi_0\frac{\mathbf{H}_{\text{eff}}}{T_1} - \frac{\mathbf{M}}{T_2} \tag{3.20}$$

When both relaxation times are set to the same value and in the limit of weak alternating fields, the resulting modified Bloch's equation, sometimes called Bloch-Bloembergen equation, is equivalent to the LL equation. The advantage of using the MBE is that the relaxation effect is treated in a different way than the LL equation (relaxation times vs damping factor).

The two separated parameters T_1 and T_2 represent the spin-lattice relaxation and the spin-spin relaxation, respectively [31]. The former is interpreted as the need of

the magnetization to reach thermal equilibrium with the surroundings and it characterizes the rate at which the M_z component of the magnetization tends towards its equilibrium position (direction of external static field). The latter is related to interactions between spins and characterizes the rate at which the transversal magnetization components $M_{x,y}$ tend towards equilibrium. However, it was shown [33] that in ferromagnets, the spin-spin relaxation component is much stronger than the spin-lattice one ($\sim 10^3-10^4\times$), therefore this last term makes almost no contribution to the absorption line width.

3.3 Spin-wave theory

Spin-waves (SW) are propagating disturbances in the magnetic ordering of the spin lattice [4]. They are associated with an ordered ensemble of spins, meaning that in many situations it is possible to apply the semiclassical macroscopic single spin model to the individual spins/domains to obtain propagation and excitation conditions. As a consequence, SW can be seen as coherent precession of microscopic magnetization vectors in a magnetically ordered material. For instance, the condition of FMR corresponds to a spin-wave mode (Kittel mode) where the spins precess in a uniform way (with wavenumber $k = 0$). SW share the same properties with other wave phenomena in nature (electromagnetic, sound, ...) like reflection, refraction, constructive and destructive interference, Doppler effect and other, as discussed in [3].

The corresponding quanta of this wave is a bosonic quasi-particle called magnon [2, 21], similar to phonons being the quanta of lattice excitations, and it carries a quantum of energy $\hbar\omega$, as well as a spin angular momentum $\hbar$. Damping and relaxation effects in FMR (cf. sections 3.2.3, 3.2.4) can be treated as collisions/interactions between quasi-particles on the magnetic system. One can distinguish intrinsic [34] and extrinsic processes [35] which contribute to the linewidth:

- On perfect crystal structures, the intrinsic processes dominate the damping rates and result in magnon-phonon interactions (thermal excitations), as well as multimagnon interactions (three and four-magnon processes being the most significant).[1]

- Extrinsic processes appear when the sample is not pure or geometrically imperfect

---

[1]For metallic and semiconducting ferromagnets, the intrinsic interaction between conduction electrons and magnons plays a significant role in the damping mechanisms (which can be two orders of magnitude greater than insulators) [36].

(e.g. rough surfaces) and results in magnon-magnon scattering, as well as rare-earth impurities scattering.

Specifically, the study of magnon damping in the ferrimagnetic insulator YIG from room to millikelvin temperatures shows a significant dependence for specific processes to dominate depending on the temperature of the material. As temperature decreases from room temperature, the contribution from intrinsic processes decrease until the main contribution is from rare-earth impurities scattering (~ 40K) [6]. Lowering even further, below 2K, incoherent losses to a bath of TLS are shown to increase the magnon linewidth [5, 37].

3.3.1 Spin-wave modes

An important characteristic of spin-waves is their dispersion relation which relates the angular frequency ω with the wavenumber k. This relation is highly dependent on the material and its geometry such that one may separate the analysis for bulk and thin films ferromagnets. The dispersion relation can be divided into separated regions due to the fact that the coupling of electron spins in magnetically ordered systems can be a result of two different mechanisms: magnetic dipolar or exchange interaction. Therefore, spin-waves can be classified into three different regions on the spectrum (Fig. 3.2):

- *Magnetostatic spin-waves*, or dipolar waves, correspond to the region of small wavenumbers. In these waves, the dipolar coupling is much stronger than the exchange counterpart. The dipolar interaction is known for its relatively low strength but very distant interaction range. For magnetic thin films, dipolar waves that propagate along an in-plane magnetized film are called Backward Volume Magnetostatic Waves (BVMSW), while waves that propagate perpendicularly are called Magnetostatic Surface Spin Waves (MSSW). Out-of-plane propagation is supported by the Forward Volume Magnetostatic Waves (FVMSW).

- *Exchange waves* correspond to the region of large wavenumbers where the exchange energy contribution is dominant. The dispersion relation of these waves is characterized by a frequency proportional to the square of the wavenumber: $\omega \propto k^2$.

- The *Dipolar-Exchange* intermediate region corresponds to an equal contribution from both the dipolar and exchange interaction to the total energy and propagation characteristics of the spin-wave.

3.3.2 Magnetostatic spin-waves (MSW)

The long wavelength regime is governed by dipolar interactions between spins which dominates when the magnon wavelength is comparable to the sample size, while exchange interactions have negligible influence on the wave properties. This means that these waves are a solution to the classical Maxwell's equations for a magnetostatic approximation (hence magnetostatic spin waves):

$$\nabla \cdot \mathbf{B} = 0 \tag{3.21}$$

$$\nabla \times \mathbf{H} = 0 \tag{3.22}$$

Assuming an applied field and magnetization of the form $H_i \hat{\mathbf{k}} + \mathbf{h}e^{jwt}$ and $M_s \hat{\mathbf{k}} + \mathbf{m}e^{jwt}$, respectively, and applying Landau-Lifshitz equation with no damping (eq. 3.2) and in the linear regime [38]:

$$\frac{j\omega}{\gamma}\mathbf{m} = \hat{\mathbf{k}} \times (M_s\,\mathbf{h} - H_i\,\mathbf{m}) \tag{3.23}$$

where $\mathbf{h}$ and $\mathbf{m}$ also follow the magnetostatic approximation: $\nabla \cdot (\mathbf{h} + \mathbf{m}) = 0$ and $\nabla \times \mathbf{h} = 0$. The latter equation means that the magnetic field can be written in the form of a scalar magnetic potential ψ ($\mathbf{h} = \nabla\,\psi$), such that the former takes the form:

$$\nabla^2 \psi + \nabla \cdot \mathbf{m} = 0 \tag{3.24}$$

From equation 3.23, the two components of the transverse magnetization can be obtained as a function of the magnetic potential ψ:

$$\frac{j\omega}{\gamma}m_x = m_y H_i - M_s \frac{\partial \psi}{\partial y} \tag{3.25}$$

$$\frac{j\omega}{\gamma}m_y = -m_x H_i + M_s \frac{\partial \psi}{\partial x} \tag{3.26}$$

and, by substituting in equation 3.24, the magnetic potential inside a spheroid sample is obtained [38]:

$$(1 + \kappa)\left[\frac{\partial^2\psi}{\partial x^2} + \frac{\partial^2\psi}{\partial y^2}\right] + \frac{\partial^2\psi}{\partial z^2} = 0 \;, \tag{3.27}$$

$$\text{with,} \; \kappa = \frac{M_s\,H_i}{H_i^2 - (\omega/\gamma)^2} \tag{3.28}$$

Taking the boundary conditions into account, the magnetostatic spin wave spectrum (dispersion relation) can be obtained for different shapes such as spheres [38] and

thin films[2, 4, 21].

Thin films MSW

There are three types of magnetostatic spin waves that may be excited in ferromagnetic thin films: surface spin waves (MSSW) and backward/forward volume spin waves (BVMSW/FVMSW), each with its own dispersion relation and properties (Fig. 3.2). The type of spin wave excited depends on the orientation of the external static magnetic field relative to the wave propagation direction.
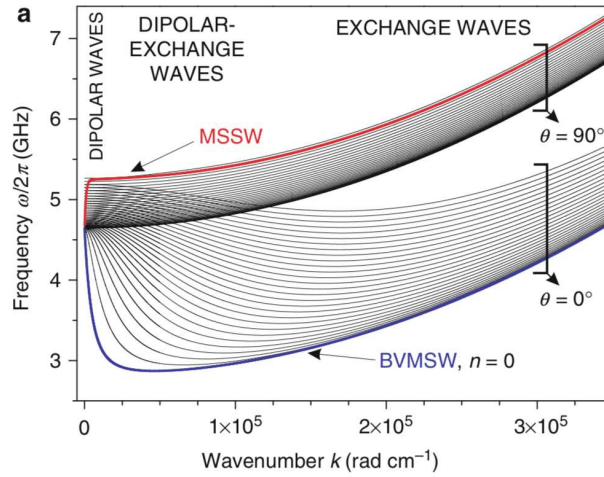
Figure 3.2: Spin-wave dispersion relation for a thin film of YIG. Three different regions of the spectrum can be identified which translate to the dominant interaction between coupled spins. Also shown are the two different spin-wave types for in-plane magnetized thin films: MSSW and BVMSW; θ is the angle between the in-plane magnetization and the direction of propagation of the spin-wave and n is the mode number. Taken from [4].

FVMSW are characterized by out-of-plane magnetization with in-plane wave propagation ($\mathbf{k} \perp (\mathbf{M}_s \parallel \mathbf{H}_0)$), whereas BVMSW and MSSW have an in-plane propagation (parallel and perpendicular, respectively) in an in-plane magnetization of the sample. An approximation for the dispersion relation of these spin waves are [2]:

$$\omega_{FVMSW} = \gamma \sqrt{H_i \left(H_i + M_s \left(1 - \frac{1 - e^{-kd}}{kd} \right) \right)} \tag{3.29}$$

$$\omega_{BVMSW} = \gamma \sqrt{H_i \left(H_i + M_s \left(\frac{1 - e^{-kd}}{kd} \right) \right)} \tag{3.30}$$

$$\omega_{MSSW} = \gamma \sqrt{(H_i + M_s/2)^2 + (M_s/2)^2 \, e^{-2kd}} \tag{3.31}$$

where k is the wave number, d is the film thickness, M_s the saturation magnetization and H_i is the internal magnetic field which includes anisotropy effects and the external bias field.

While at low wavelengths (exchange waves) the dispersion follows a parabolic curve where the frequency increases with the square of the wavenumber, at high wavelengths (magnetostatic waves), their behaviour is very distinct. The main difference is in the group velocity of the waves (seen by the slope of the curve): BVMSW have a negative group velocity, meaning that when the wavelength decreases the frequency decreases as well (and vice-versa), whereas MSSW have a positive group velocity.

Chapter 4

Room temperature FMR setup

To measure ferromagnetic resonance (FMR) at room temperature, a typical magnetic resonance setup was assembled which consists of a strong static magnetic field to saturate the magnetization of the samples and a microwave generator to excite the resonance phenomenon. In this section, an overview of this system will be provided, with a detailed description of each component, as well as of the samples tested.

4.1   System description and components

As explained in chapter 3, FMR occurs when a ferromagnetic system absorbs microwave energy which matches the resonance condition (eq. 3.8), macroscopically corresponding to a uniform precession of the spins around the direction of the external magnetic field. The diagram shown below (Fig. 4.1) represents the setup used and consists of three main components: VNA, electromagnet and hall probe.

4.1.1   Vector Network Analyser

To generate the microwave signal necessary to excite the magnetization vector, a *Rohde & Schwarz* ZVA40 Vector Network Analyzer (left Fig. 4.2) was used to perform transmission measurements through a copper microstrip in a $30{\times}30$ mm^2 printed circuit board (PCB) which was connected to both ports of the VNA using $50\ \Omega$ matched microwave-rated coaxial cables and SMA connectors.

The nature of these experiments did not require the full use of a vector analyser, since we are mostly interest in amplitude variations when the ferromagnetic system

absorbs part of the energy in the microstrip. Nonetheless, the phase data is always useful to confirm the FMR frequencies and to perform complex fitting routines.
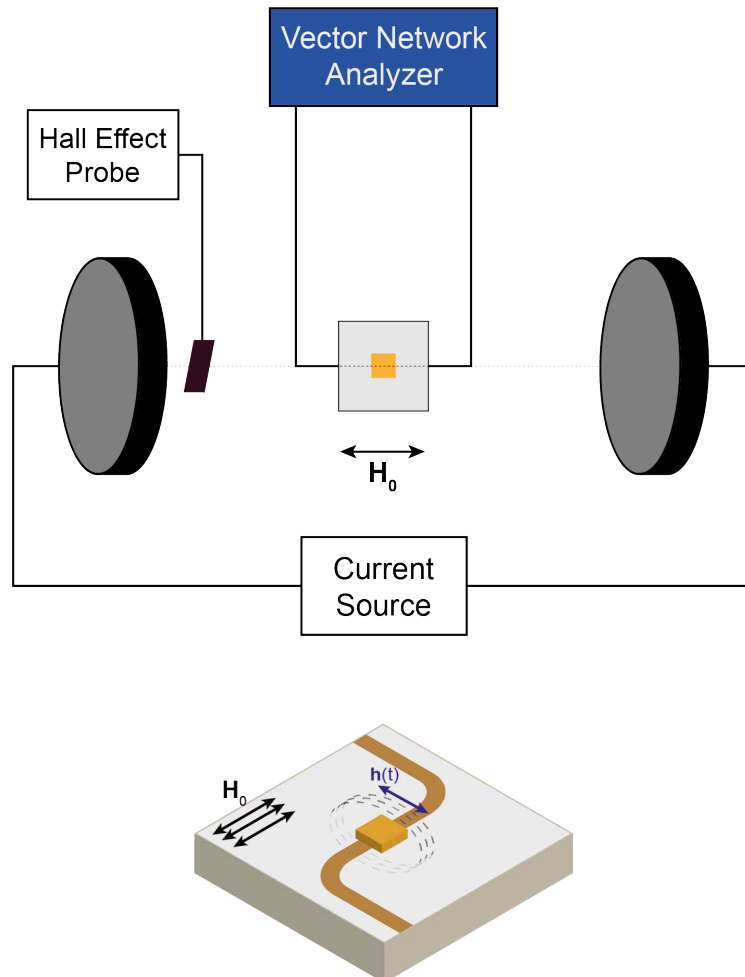
Figure 4.1: Diagram of VNA-FMR setup used for room temperature experiments. Three main components can be identified as the VNA, the electromagnet and the hall probe sensor. Bottom picture shows a detailed view of the transmission line with the a YIG sample on top, together with a visualization of static and alternating magnetic fields.

4.1.2   Electromagnet

The static magnetic field was generated using a *GMW* 3470 dipole electromagnet which can create uniform fields up to 1 T between two cylindrical plane face poles (40 mm diameter), depending on the distance between these poles and the type of pole used (plane or tapered faced). These poles are mounted in the middle of Helmholtz coils (right Fig. 4.2) and they guide the field inside them, due to high permeability μ_r of the material used for both poles.

This magnet is powered by a *Kepco* BOP 100-10MG current supply, delivering to

the magnet up to a maximum of 6 A. This upper limit can be reached when the magnet is water cooled, to prevent overheating and damage to the system.

4.1.3 Hall effect probe

To measure the effective magnetic field created, a *MAGSYS* HGM09 hall effect sensor was mounted on the magnet, as close as possible to the sample. With this instrument, it was possible to determine a average current to field ratio around 72 mT/A, where variations in the ratio between experiments are mostly attributed to hall probe not being equally and perfectly aligned and placed in the mount.

Figure 4.2: Picture of instruments used in room temperature setup: (left) VNA and (right) electromagnet with hall probe.

4.2 Transmission lines

Two transmission lines were used in this work, corresponding to two different PCBs with distinct substrates (Fig. 4.3). Both had 50 Ω matched SMA connectors which connected to the VNA ports. First one used was an S-shaped microstrip line with mitered bends to prevent parasitic reactances at discontinuities such as right-angle corners. Unfortunately, the substrate was unknown and its performance above 5 GHz was poor, reason why a second transmission line was designed and fabricated.

Second one was an S-shaped (swept bends) copper microstrip line on TMM10 substrate. It consists of a ceramic polymer composite, well known for its microwave frequency performance [39]. In order to avoid impedance mismatches between the coaxial cables and the transmission line itself, the microstrip was designed such the width of the line corresponded to a 50 Ω impedance. To do so, the following formula

for a microstrip line was used [8]:

$$\frac{W}{d} = \frac{8e^A}{e^{2A} - 2} \quad , \text{ for W/d } < 2 \tag{4.1}$$

with

$$A = \frac{Z_0}{60}\sqrt{\frac{\epsilon_r + 1}{2}} + \frac{\epsilon_r - 1}{\epsilon_r + 1}\left(0.23 + \frac{0.11}{\epsilon_r}\right) \tag{4.2}$$

The substrate used was characterized by a relative permittivity $\epsilon_r = 9.8$, substrate thickness of $d = 0.381$ mm and copper thickness of $w_c = 17$ µm. The desired impedance was $Z_0 = 50$ Ω.
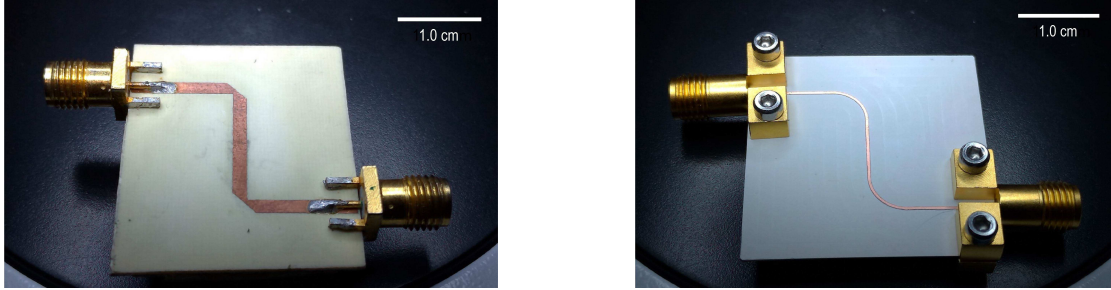
Figure 4.3: Two different transmission lines (and PCBs) used in this work: (left) S-shaped mitered microstrip (#1) and (right) S-shaped curved microstrip with TMM10 substrate (#2).

4.3 Samples

Samples used throughout this work were made of the same material: YIG. Yttrium Iron Garnet ($Y_3Fe_5O_{12}$ - YIG) is a synthetic ferrite crystal known for its ferrimagnetic insulating behaviour which results in magnetic properties such as very low spin-wave damping coefficient, as well as showing the narrowest known FMR curve [40]. Its unit cell consists of 80 atoms in a cubic structure, where 20 of them are magnetic ions (Fe^{3+} in two different geometric sites) responsible for the strong exchange interactions (antiferromagnetic with different exchange constants) that dominate the magnetic order in YIG. At low energies, this ordering can be considered ferromagnetic and spins precess essentially in phase with each other.

As seen in chapter 3, the shape of the sample plays a big role in the effective magnetic field that is perceived by the magnetic moments in the material. It is also known that for thin films, higher mode magnetostatic spin-waves can be more easily probed due to the non-uniform field distribution that excites $\mathbf{k} \neq 0$ magnons. Therefore, two different YIG shapes were probed: a sphere and a rectangular thin film.

First, a 0.5 mm diameter YIG sphere (left Fig. 4.4), mounted on the (110) axis of a ceramic rod, from *Ferrisphere, Inc.* was used. The YIG thin film (right Fig. 4.4) was fabricated by epixatial growth on a Gallium Gadolinium Garnet (GGG) substrate aligned with (111) direction, which resulted in a 0.99 µm thick film with lateral dimensions of $\sim 3 \times 3$ mm^2. Results for both samples can be seen in section 6.1.
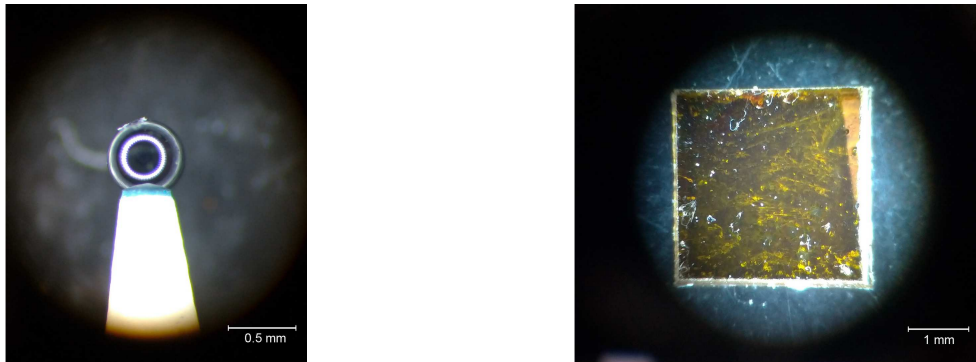
Figure 4.4: YIG samples used in this work: (left) sphere and (right) thin film.

Chapter 5

Adiabatic Demagnetization Refrigerator for milliKelvin measurements

Superconducting circuits require low temperatures to operate, ideally much lower than their critical temperature T_c. If operating in the quantum regime, even lower temperature need to be achieved to minimize the thermal noise in the system ($k_B T \lesssim \hbar \omega$). This chapter is concerned with the setup used to achieve such temperatures, as well as the measurement system necessary to extract physical information out of these circuits.

The Adiabatic Demagnetization Refrigerator (ADR) used in these experiments was a *Entropy ADR Cryostat M-Series* and it enabled us to reach milliKelvin (mK) temperatures by converting magnetic to thermal entropy, and vice-versa, to adiabatically cool down the sample holder. A detailed overview of its operation is given, as well as a description of the engineering component of such system.

5.1 Principle of operation

The main components of an ADR include:

- Double-stage salt pill unit - paramagnetic material, usually a salt, such as Ferric Ammonium Alum (FAA) and/or Gallium Gadolinium Garnet (GGG), whose disordered magnetic moments can be used to convert magnetic entropy to thermal.

- Superconducting magnet - controls the magnetic field applied to the paramagnetic salt and, consequently, the energy conversion.

- Heat switch - controls the heat flow between the salt unit and the 4 K stage of the ADR which acts as a thermal sink for the heat produced at the salt.

The cooling cycle starts with the heat switch closed and the salt unit at thermal equilibrium with the 4K stage. The magnet is slowly ramped up to a current of ~ 40 A with a resulting magnetic field which magnetizes the salt, aligning the magnetic moments with it. This process heats up the salt pill due to the decrease in magnetic entropy (lower disorder) which is converted to thermal entropy (higher temperature). The excess heat is dissipated at higher stages and when thermal equilibrium is established once again, the heat switch is opened (adiabatic process) and the current can be reduced gradually. As the external magnetic field decreases, the magnetic moments return to the disordered state by absorbing heat from the sample (increase in magnetic entropy and decrease in thermal). When the magnetic field disappears (current reaches 0 A), the ADR no longer has any cooling power available and the system starts warming slowly up due to heat leaks from the surroundings.

This means that this type of refrigerator is not able to maintain the minimum temperature achieved for much longer, as opposed to a dilution refrigerator. Instead of consuming all the cooling power available from the demagnetization all at once, it is also possible to defined a certain temperature (above the minimum base temperature achievable) and the cryostat is able to regulate the decrease of current remaining as to maintain that specified temperature, using a PID (proportional-integral-derivative) control system.

A visualization of this procedure is illustrated in Fig. 5.1 with the help of a entropy S vs temperature T graph.

5.2   System description and components

The ADR cryostat is separated into four stages: 70 K, 4 K, GGG (500 mK) and FAA (base temperature, ~ 30 mK) stage. The demagnetizing unit works at the GGG and FAA stages, while the 4 K and 70 K stages acts as a heat sink to start the procedure. These stages serve to distribute the cooling power from room temperature to mK, by applying different cooling mechanisms: first, a pulse-tube cryocooler is used to reach sub 4 K temperatures (around 3 K), then, the demagnetization mechanism lowers the temperature further to mK regime.
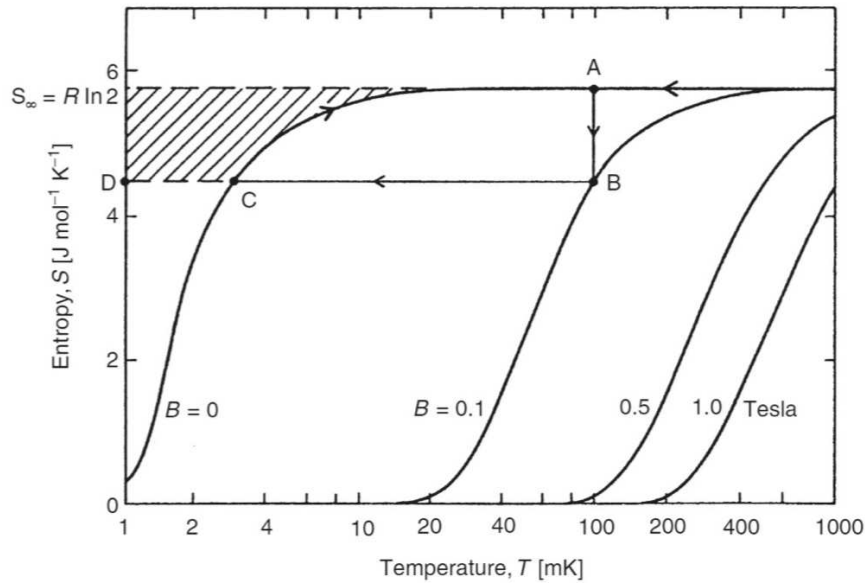
Figure 5.1: Thermodynamical cycle of adiabatic demagnetization of a single crystal of a paramagnetic salt. In the entropy S vs temperature T graph, this cycle can be visualized by the A-B-C path, where the salt start in a disordered high temperature state (A) and then the magnetic field is increased which results in a decrease of magnetic entropy (B), while keeping the thermal contact to the heat sink. After the heat switch is opened, the magnetic field is reduced and the temperature drops (C) adiabatically (from Ref. [41]).

The different subsystems of the ADR can be seen in Fig. 5.2.
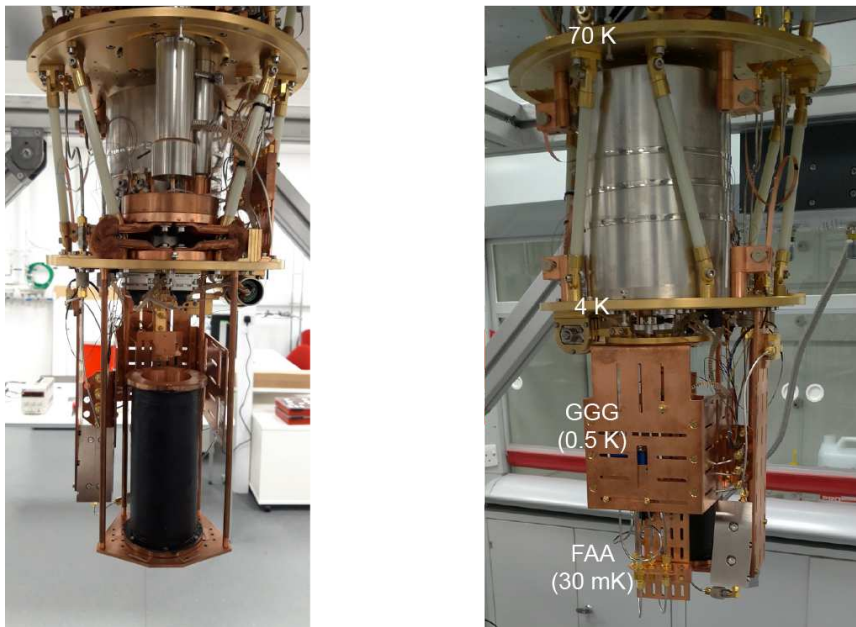
Figure 5.2: Detailed view of different stages inside the ADR. Four temperature stages can be seen corresponding to 70 K, 4 K, GGG and FAA. The salt pill unit can be seen on the right, between the top two stages (grey cylinder).

5.2.1 Vacuum System

To seal the whole system, a two-stage vacuum system is employed. The ADR main stages are kept inside a vacuum shield and the air is extracted from the system using a serial combination of two distinct pumps. First, a roughing pump starts the initial air evacuation until a certain pressure (for our system, ~ 50 mbar) at which point, a turbomolecular pump is activated.

A turbo pump works on the principle of momentum transfer between a set of angled rotor blades inside the pump and the air molecules arriving from the cryostat. As the transfer of momentum occurs, the molecules travel to the next stage of rotor blades, where the same process happens, until it reaches the exhaust stage. This stage is connected to the input of the roughing pump such that the molecules can be extracted.

Since the system is at cryogenic temperatures, another phenomenon occurs where the air molecules condense onto the surface of the cold parts, effectively lowering the pressure even further (cryotrap). Overall, pressures of $\sim 10^{-7}$ mbar are achieved using this system.

5.2.2 Pulse Tube Cryocooler

The pulse tube (PT) precooler used is a two-stage GM-type consisting of a room-temperature compressor, valve unit and cold head. This precooler is responsible for setting the temperatures of the 70 K and 4 K stages, as well as maintaining them constant throughout the duration of the experiment. This system is initiated when the pressure inside the ADR is close to 10^{-3} mbar.

The cooling effect is achieved at the low temperature heat exchanger X_L (Fig. 5.3) by compressing the working gas which leaves X_L at low temperature and allowing it to expand and return to X_L with a lower temperature [42]. The alternating pressure (which compresses and expands the gas) in a GM-type PT results from a valve switching from the low and high pressure sides of the compressor unit. The working gas is Helium (^{4}He) because it is a great approximation to an ideal gas, but more importantly, it has a very low condensation temperature ($\sim$4.2 K for ^{4}He, $\sim$3.2 K for ^{3}He), which makes it possible to reach these temperatures.

However, the system uses a two-stage PT, where the first stage precools the second one, which can then reach lower temperatures than just a single stage PT. In the ADR system, the first stage corresponds to the 70 K ADR stage (real temperature is actually lower, ~ 50 K) and the second stage is the 4 K stage (also lower, ~ 3

K). The major advantage of PT cryocoolers is the fact that a bath of liquid helium is not required to reach 4 K temperatures which, not only significantly lowers the cost of operation, but also enables the design and operation of more compact and robust dilution and adiabatic demagnetization refrigerators ("cryofree").
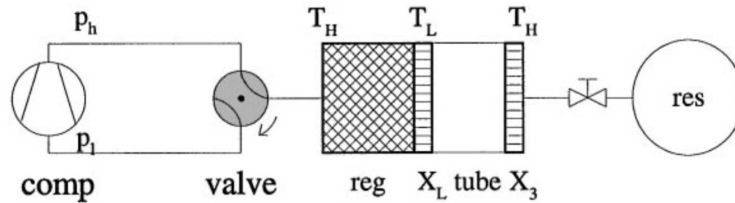
Figure 5.3: Diagram of GM-type Pulse Tube cryocooler. From Ref.[42].

5.2.3 Temperature Stages

Thermal properties of the wiring

The four temperature stages should, in theory, be thermally isolated from each other such that the temperatures remain constant and at the desired values. However, the stages are indirectly connected by the wiring required for DC and microwave components at lower stages.

The materials used for the wiring depend on which stage they will be used in and on the need to connect different stages. DC wiring mainly consists of Beryllium Copper (BeCu) wires from room temperature to 4K stage, followed by superconducting NbTi wire to the lower stages. These wires form a twisted pair to reduce electromagnetic noise and are thermally clamped between each stage to thermalize the wire.

Microwave wiring consists of semi-rigid stainless steel (SS) coaxial cables which have relatively low thermal conductivity to minimize the passive heat load between stages (heat that flows from higher to lower temperatures) and also have good microwave transmission properties. If the wiring is connecting components at the same stage, flexible cables (CuNi) are used, despite having slightly higher passive heat load, since in the same stage the passive load should be zero. Superconducting coaxial cables can also be used (NbTi) which minimize the passive load, as well as the active load which consists of ohmic losses of microwave signals in the attenuators and wires (section 2.3.2).

Radiation isolation

To protect the samples from radiation loads, two thermal shields are used at 70 K stage and at 4 K stage. Both shields are made of Al (Aluminium), but at 4 K stage the shield is gold-plated to reduce oxidation (corrosion). The goal of the thermal shields is to reduce the radiation thermal load (especially infrared radiation) on the system due to blackbody radiation by having a very low emissivity material. This thermal load is more significant at higher temperature stages (e.g. 70 K) [43].

Sample mounting

Samples are mounted on a sample box through a wire bonding technique to connect the pads on the circuit to the outside connectors. This box is then installed at base temperature stage and the connections to the microwave circuit are made through the SMA connectors on the box.

5.2.4 Electronics Rack

The electronics rack centralizes the remote control of components of the ADR such as the compressor unit, heat switch, current source for superconducting magnet of the demagnetization unit and gathers all data from instruments such as temperature sensors and pressure gauges.

As briefly mentioned before, the electronics of the system can be divided into DC and microwave circuitries. DC wiring going into the cryostat include power supplies for instruments (e.g. microwave switch, cryogenic amplifiers, heat switch motor), current supplies for superconducting magnets (both the internal magnet and the solenoid for FMR experiments, section 5.3). The microwave circuitry comprises everything between the two ports of the external VNA and it is the fundamental measurement system for superconducting quantum circuits experiments (section 5.4).

5.3 ADR Solenoid system for FMR measurements

5.3.1 Design and fabrication

To perform FMR measurements at milliKelvin temperatures, a static magnetic field is required to saturate the magnetization of the YIG material in one direction, while

a perpendicular microwave field excites the resonance. Therefore, we designed and fabricated the solenoid with the main requirement of providing a field of 500 mT to the sample (at base temperature) with a 6 A current[1].

Assuming a finite length of solenoid, the number of turns and layers for specific wire diameter can be obtained through Ampere's law. The spool made of copper had been previously designed for an effective length of 15 cm with 5.2 cm diameter and fabricated from a mechanical workshop. The wire used to make the solenoid was superconducting NbTi in Cu matrix with diameter of 0.33 mm. Using this diameter, the total number of layers needed was calculated to be around 22 for a total length of wire of about 1850 m.

The winding was done manually using a winding machine (see Fig. 5.4) powered by a low frequency DC motor which could be adjusted to different winding speeds. Between every two layers, thermally conductive epoxy (stycast) was applied to secure the wires due to the magnetic forces exerted on them during operation and to thermalize the solenoid more easily, while at the same time maintaining electrical isolation. This Stycast 2850FT consists of two components, resin and catalyst, which are mixed by weight ratios 100:3.5, respectively, and produce a black-coloured mixture. Before applying, we outgassed the epoxy using a desiccator with a vacuum pump to remove air that was incorporated during the mixing phase. After applying, the stycast takes about 12 hours to fully dry. After the solenoid was wound, a simple resistance measure was performed to ensure there were no breaks in the wire and the final resistance was measure to be around 800 Ω, consistent with copper resistance at room temperature (at this temperature, NbTi resistance is higher than copper).

---

[1]Note: ADR rely on high magnetic fields to perform the cooldown operation which would obviously influence any FMR measurements. Therefore, it is important to notice these two systems are operated while the other is OFF: the cooldown is performed with zero current on the FMR solenoid and FMR measurements are performed when the current on the ADR magnet is low ($\sim$ 0.5 A). Even then, there is a magnetic shield around this magnet which guides the remaining low magnetic field inside.

Figure 5.4: (Left) Finished solenoid mounted on the winding machine with final layer of stycast applied. (Right) Close up of the superconducting NbTi wire during the winding process.

5.3.2 Wiring and mounting

The solenoid was attached to the 4 K stage of the ADR through a copper mount previously designed and fabricated specifically for this solenoid (Fig. 5.5). In case an electrical short appeared between the grounded spool and the first layers of the wire, the solenoid was electrically isolated from the mount using small sapphire wafers and plastic screws which could have slightly decreased the cooling efficiency. Still, since the magnet is operating at 4 K, all current supplied should go through the superconducting wire since it offers zero DC resistivity.

The wiring of the magnet from room-temperature requires special attention due to the fact that there will be normal current (> 6 A) going inside and superconducting current reaching the solenoid. With this fact in mind, the wiring was designed to minimize the heat load to the superconductors (preventing them from "quenching"), by dividing it in three stages: copper, high T_c superconductor (HTS) and low T_c superconductor (LTS) (Fig. 5.5)

The current supply is connected to the inside of the ADR using copper wires which continue until the 70 K stage. At this stage, a thermal clamp is used to "bond" the HTS (ReBCO tape, Rare earth-Barium-Copper Oxide) with the copper wire, providing the electrical connection and the thermalization required to dissipate the heat from the "normal" current carried by copper wires. After this step, current is now carried by Cooper pairs in superconductors, therefore removing the active heat dissipation to the lower stages. Again at the 4 K stage, another thermal clamp "bonds" the HTS with the LTS wire from the solenoid (NbTi) and the circuit is closed by repeating the same procedure from the solenoid to room temperature.
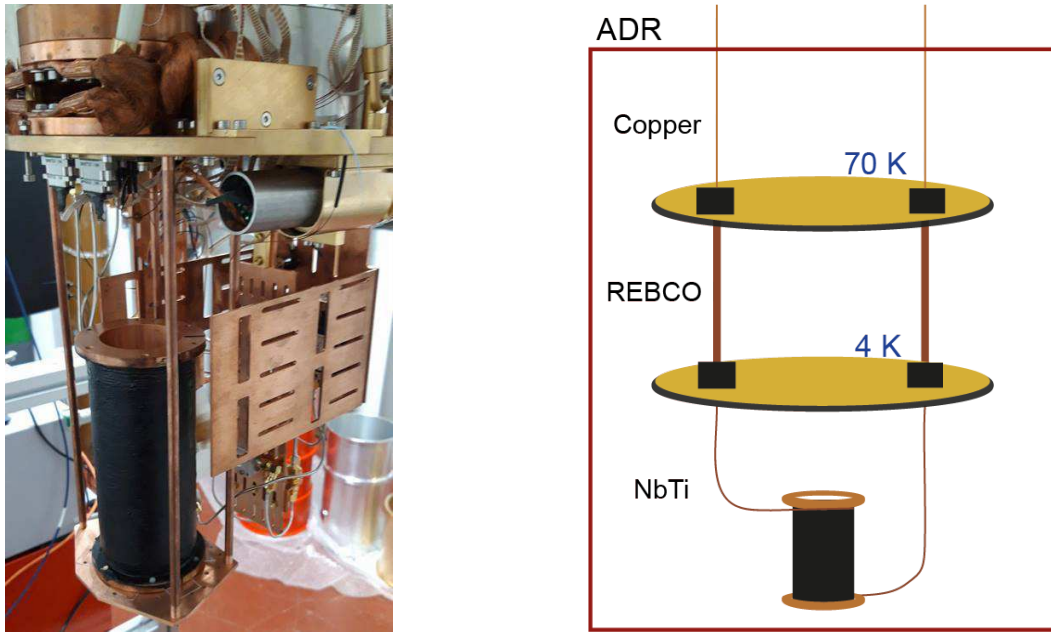
Figure 5.5: (Left) Solenoid mounted at the 4 K plate of the ADR using pillars to support it from the top. (Right) Wiring diagram of the solenoid starting from the external current source (copper wires) to the lowest stage (superconducting wires). Black boxes represent thermalization clamps in each stage which "bond" the different wires.

5.3.3 Testing and calibration

The first solenoid tests were done at ~ 3 K to ensure the superconductivity of NbTi ($T_c \sim 10$ K) while the current was ramped up to the desired value of 6 A. To minimize the power dissipated in the first stages of the wiring ($P = IV = I\dot{I}L$), the current increase rate was low (0.01 A/s). This rate was also important to prevent the quenching of the magnet, i.e., the sudden change from superconducting to normal state, which would dissipate most of the energy from the high currents, heating up the entire ADR. After the current was set to 6 A and no signals of quenching, we increased the current further to 10 A and, still, the magnet was fully functional.

Specifically for our experiments, the characteristics that we were interested in were the values of magnetic field that could be predicted inside the solenoid, as well as its homogeneity. To get a current to magnetic field conversion, we gathered data of the response of a paramagnetic sample (organic molecule, DPPH) on top of a transmission line to a frequency and current sweep. For every 0.01 A supplied to the solenoid, the VNA would do a 2-18 GHz sweep with 2 MHz of resolution. The results of this measurement can be found in appendix B.

5.4 Microwave measurement system

The measurement system consists of the microwave instrumentation necessary to probe the quantum systems inside the cryostat. The main component of the setup is the VNA which generates the input microwave signal to the sample and receives its output for vector network analysis (section 2.2). It can be divided into passive and active components.

5.4.1 Passive components

Attenuators

This signal has to be heavily attenuated before reaching the sample box at mK temperature, mainly due to active thermal load issues, i.e. to reduce thermal noise (Johnson-Nyquist) such that the number of thermal photons at the sample is well below 1. Secondly, if the experiment requires reaching quantum regime where there is on average a single microwave photon on the resonator, even higher attenuation is required (>100 dB).

Therefore, three stages of attenuation are implemented after the output of the VNA consisting of 20dB attenuators at 70 K, 4 K and 0.5 K (GGG) stages with the main goal of reducing thermal noise (total of 60 dB plus the attenuation of coaxial cables and insertion loss of other microwave components). The total attenuation wanted (60 dB) is cleverly distributed among stages and optimized in such a way that the active load reaching a lower stage is well below the cooling power available for that stage [43].

DC blocks

On both input and output lines, DC blocks with frequency range of 10 MHz - 18 GHz are installed between some components as basic high-pass filters to block all DC connections between stages, as well as low-frequency noise (e.g. from PT valve unit and $1/f$ noise). This is especially important for monitoring the heat switch mechanism in the ADR, since wiring connects all stages and therefore the resistance between 4 K and lower stages would always be close to 0 Ω, whether the actual switch was opened or closed.

Isolators

After the sample, at 4 K, a cryogenic rated double junction isolator operating from 4 - 12 GHz with a minimum isolation of 24 dB is placed to prevent noise coming from upper stages from reaching the sample. This device is magnetically shielded (high permeability material) from the outside to ensure the internal ferrite component is not biased by an external field which would degrade its performance.

This two-port non-reciprocal microwave component ideally transfers all power from one direction, but blocks all from the opposite. It is a special case of a circulator which is a three-port device where power flows in a certain clockwise or counter-clockwise direction, but not the opposite way. By matching one of the three ports with a 50 Ω load, no power is lost at this port and the device becomes an isolator.

5.4.2 Active components

Microwave switch

Before the isolator, at 0.5 K (GGG), a two output latching microwave switch, with SMA connectors up to 18 GHz and switching times of 10 ms, is used so that in each cooldown of the ADR two samples can be measured simultaneously. The power pins are connected to a room temperature power supply box through copper wires until 4 K, then NbTi in Cu matrix is used to complete the wiring. To switch between samples, two buttons in the external box are implemented to send signals which activate the solenoid actuators and perform the switching action.

HEMT amplifier

After the isolator, at 4 K, a cryogenic High Electron Mobility Transistor (HEMT) amplifier provides low-noise and high gain amplification of the attenuated signal coming from the sample with a bandwidth of 4 to 16 GHz. Typical gains values are around 35 dB with a noise-temperature around 3 K. Power supply wiring for this component is done the same way as for the switch, with copper and NbTi.

This type of transistor outperforms traditional MOSFET and MESFET in terms of high frequency operation due to the high electron mobility of the 2D electron gas formed in the heterojunction of two different semiconductors (e.g. GaAs and AlGaAs). Properties such as the electron mobility and thermal noise can be further improved by working at cryogenic temperatures.
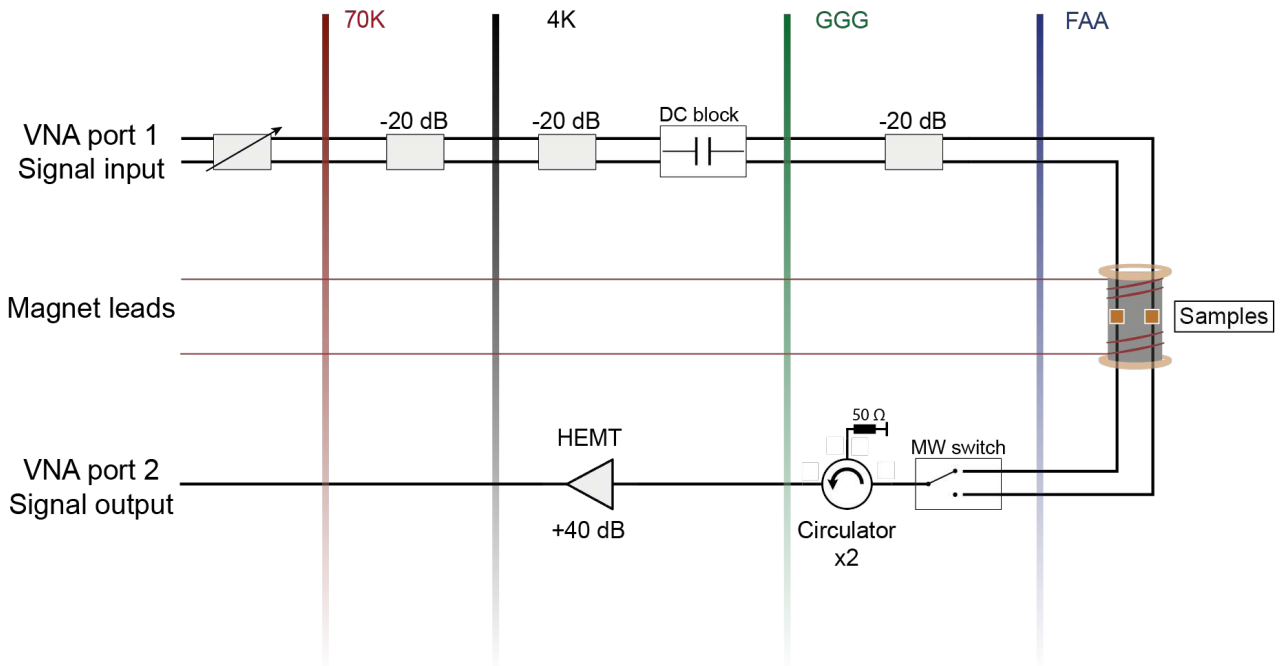
Figure 5.6: Microwave wiring inside ADR. Signal generated by VNA is fed through layers of attenuation and filtering before reaching the sample at milliKelvin. On the way out, this signal passes through an isolator and an HEMT amplifier before entering the other port of the VNA. Magnet current leads also enter the ADR, as shown in Fig. 5.5, to power the superconducting solenoid.

5.5   PFIB YIG samples

YIG samples used for milliKelvin experiments were fabricated by deposition with a Plasma Focused Ion Beam (PFIB) technique [7]. This deposition is accomplished by creating a focused ion beam (with this tool, a Xenon plasma beam) which enters a vacuum chamber where the sample's substrate is located and allowing a precursor organometallic gas to flow in. As the gas enters (at controlled pressure and flow), the beam breaks down the molecules into the non-volatile desired material to deposit (YIG) and a volatile gas which is pumped out of the chamber. The metal is deposited on the substrate, with a specific rate, as the beam is scanned in the desired pattern to create 3D structures with great spacial resolution.

Two samples fabricated this way were tested in this work with dimensions of $\sim$ $50{\times}50{\times}10$ µm^3 and $\sim 50{\times}10{\times}5$ µm^3 (Fig. 5.7). These two dimensions were chosen

carefully (as will be seen later), as well as the placement of these YIG cuboid shaped samples on top of a CPW superconducting transmission line. The larger sample was wide enough to cover both ground planes, while the thinner one had about the same width of the central conductor and was, therefore, placed on top of it. To secure the samples to the transmission line, platinum was deposited on the borders. A third sample was fabricated with same dimensions of $50{\times}50{\times}10$ µm^3, but placed on top of a CPW inline $\lambda/2$ resonator which was fabricated on the same chip as the sample on the transmission line.
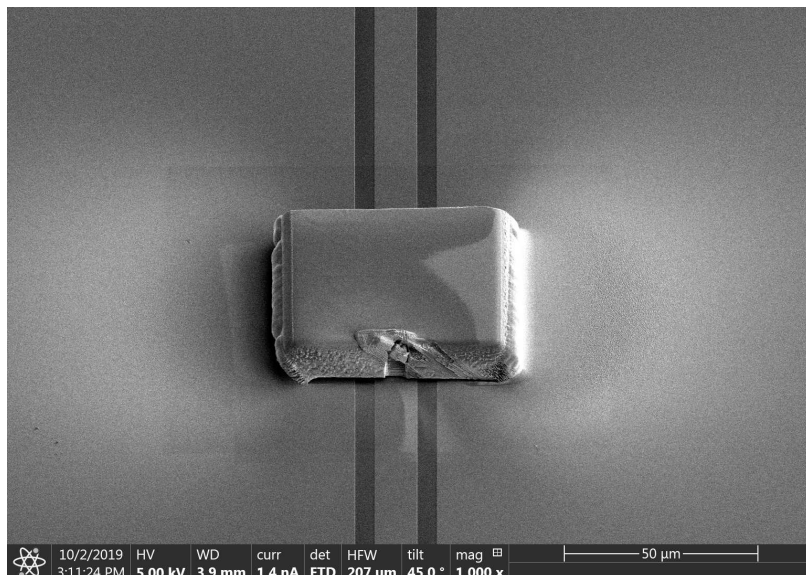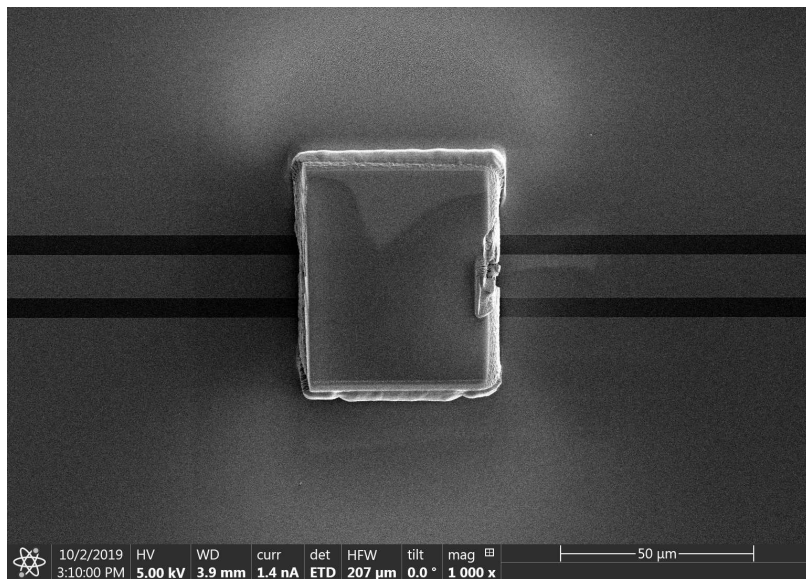
Figure 5.7: Example of a PFIB YIG sample with dimensions of $50{\times}50{\times}10$ µm^3 placed on top of a NbN CPW transmission line. Borders are sprayed with platinum to "glue" the sample to the chip. Micrograph taken with SEM at the Kelvin Nanocharacterisation Centre, School of Physics & Astronomy, University of Glasgow.

Chapter 6

Results

6.1 Room temperature

This section is dedicated to the results obtained for FMR measurements at room temperature using the setup and samples described in chapter 4. Detailed spectroscopy measurements were realized to obtain the FMR curve, as well the dispersion relation for higher order magnetostatic spin waves, from which the gyromagnetic ratio and saturation magnetization (for thin films) could be determined. Other characteristics of magnetic materials were also studied such as the Gilbert damping factor, anisotropy and hysteresis effects.

6.1.1 FMR spectra

To start characterizing spin waves (specifically, the Kittel mode), a full sweep of magnetic field and VNA frequency was made to obtain the spin-wave spectrum (S_{12} or S_{21} transmission) for both the YIG sphere and thin film. The result of such measurements can be seen in Fig. 6.1 and Fig. 6.2, where data was taken for microstrip #1 and #2, respectively.

From these first results, it is possible to see the impact of shape on the dispersion relation of magnons in YIG (section 3.2.2). Another important feature seen is the excitation of higher order magnetostatic spin wave modes, where this characteristic is much clearer using microstrip #2. The explanation resides on the fact that this PCB has a much narrower trace width due to the high dielectric constant of the substrate.

For the sphere, this means that the line is of the same dimension of the diameter and

the AC fields created are no longer homogeneous inside the sphere. This condition
of non-homogeneous fields is required to excite $\mathbf{k} > 0$ spin waves which are seen in
the data. For the thin film, the trace width is smaller than both lateral dimensions
of the film which means the AC magnetic field mostly excites local spins and not
the entire sample in a uniform manner. Therefore, spin waves are created and
propagated in the film, corresponding to backward volume (BVMSW) and surface
spin wave (MSSW) modes (section 3.3.2).
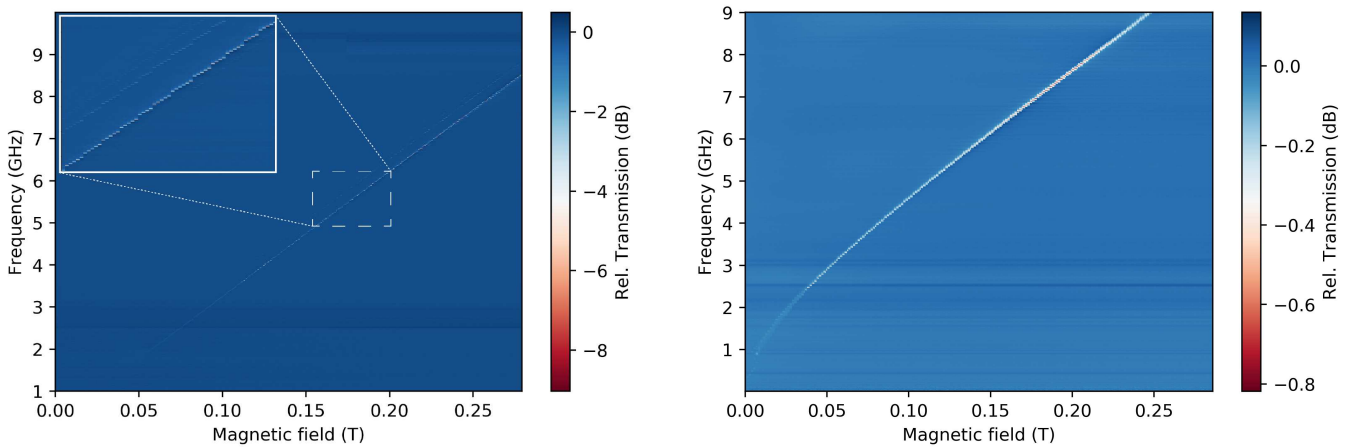
Figure 6.1: [PCB #1] FMR sweeps for YIG sphere (left) and thin film (right). For both measurements, current was swept from 0 to 4.00 A (0.01 A step), while VNA frequency was swept from 1-10 GHz (2 MHz step) and 0.01-9.01 GHz (2 MHz step) for sphere and film, respectively. IFBW was set to 1 kHz. Data presented is processed by subtracting the background transmission at zero field.
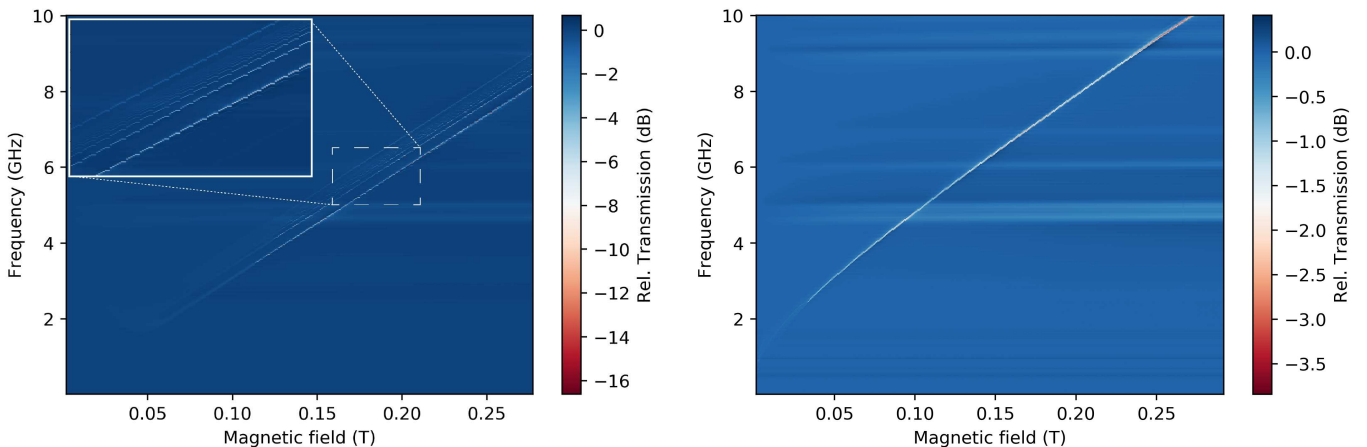
Figure 6.2: [PCB #2] FMR sweeps for YIG sphere (left) and thin film (right). Current was swept from 0 to 4.00 A (0.01 A step) , while VNA frequency was swept from 0.01-10.01 GHz (1 MHz step). IFBW was set to 1 kHz. Data presented is processed by subtracting the background transmission at zero field.

Despite being difficult to see the curve on a surface plot (specially for the YIG sphere), it means the transmission dip due to FMR is extremely narrow (very low linewidth), while the absorption amplitude is also quite deep (from -16 to -8 dB). This characteristic of YIG will be studied in detail in section 6.1.2. For thin films, the absorption is not as deep which is a result of weaker coupling of spins to the microstrip, as well as the lower number of overall spins in the system due to the much smaller volume.

6.1.1.1   Sphere analysis

Using the Kittel formula for spheres (equation 3.3), a linear fit was performed to extract the gyromagnetic ratio γ for both transmission lines used (Fig. 6.3).
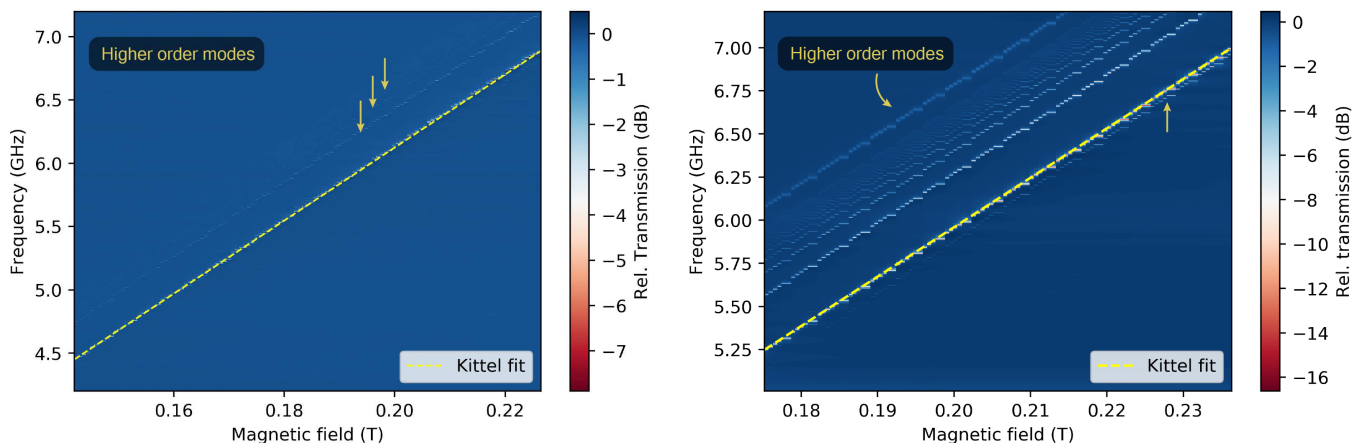
Figure 6.3: [Left] FMR curve for YIG sphere 0.5mm diameter in PCB #1. Zoom of the curve for magnetic fields between 0.15 and 0.22 T shows other magnetostatic modes (Walker modes) present together with main Kittel mode. Fit to Kittel mode resulted in $\gamma = 28.76 \pm 0.02$ GHz/T gyromagnetic ratio, as well as an offset $\omega_{\text{off}} = 0.344 \pm 0.003$ GHz. [Right] FMR curve for same sphere in PCB #2. Even stronger excitation of Walker modes leads to rich spectrum with plenty of dispersion curves. Fit to Kittel mode resulted in $\gamma = 28.634 \pm 0.007$ GHz/T gyromagnetic ratio, as well as an offset $\omega_{\text{off}} = 0.233 \pm 0.001$ GHz.

The values of gyromagnetic ratio γ match the expected value of 28 GHz/T very well (Table. 6.1), despite the small error mainly attributed to fluctuations of the magnetic field and also the fact that the measured field was measured slightly above the sample, therefore the current to field conversion determined is not exactly equal to the one felt by the sample. The offset frequency ω_{off}, also known as the zero field resonance frequency, is thought to be a result of small hysteresis of YIG which, as the external field is swept back to zero, maintains a non-zero magnetization which interacts with the microwave photons and produces the residual resonance effect.

As explained previously, not only the Kittel mode is excited in this setup, but also other magnetostatic spin waves. For spherical samples, these modes are called Walker modes [38] (Fig. 6.4) and they are represented by indices (n,m) which correspond to different Legendre polynomial solutions to the magnetostatic potential equation 3.27. Using this notation, (1,1) is the Kittel mode and it can be shown that, like many other modes, it is intrinsically degenerate to higher modes (for instance, (4,3) has the same dispersion relation as (1,1)).
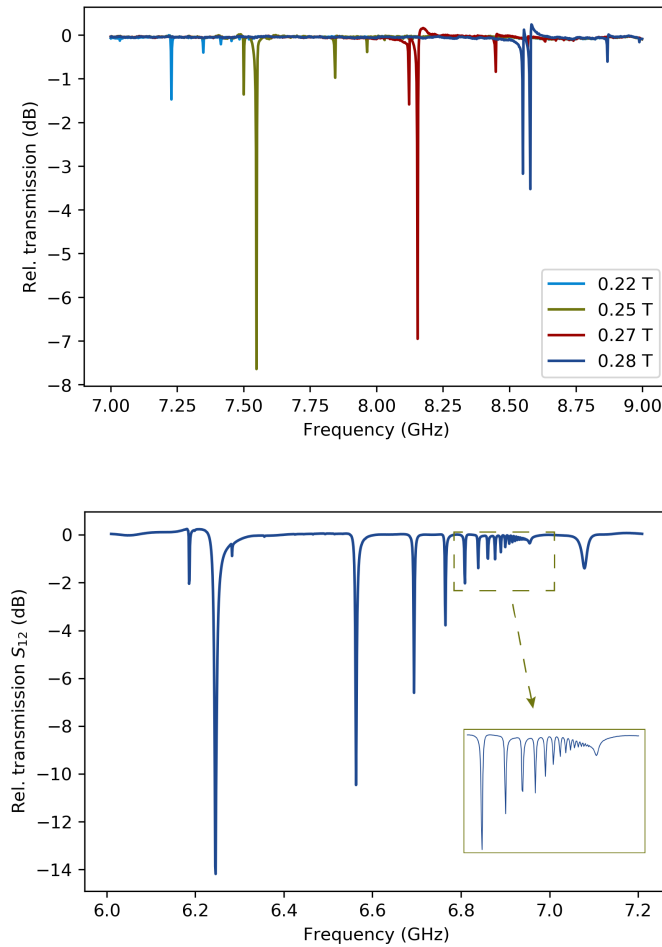
Figure 6.4: [Top, PCB #1] Transmission spectrum at different fields show the sharp dips of transmission corresponding to Kittel mode (largest absorption) and a few Walker modes. [Bottom, PCB #2] Spectrum at $H = 210$ mT shows the increase of Walker modes excited by reducing the microstrip width. Largest peak corresponds to Kittel mode.

6.1.1.2 Thin film analysis

Doing the same analysis for the YIG thin film, a fit was also performed on the FMR curve using a modified version of equation 3.9:

$$\omega = \gamma\sqrt{(H + H_a)(H + M_s + H_a)} \tag{6.1}$$

to include the effects of anisotropy fields (which are known to be small in YIG samples). The result of this fit for both transmission lines can be seen in Fig. 6.5.
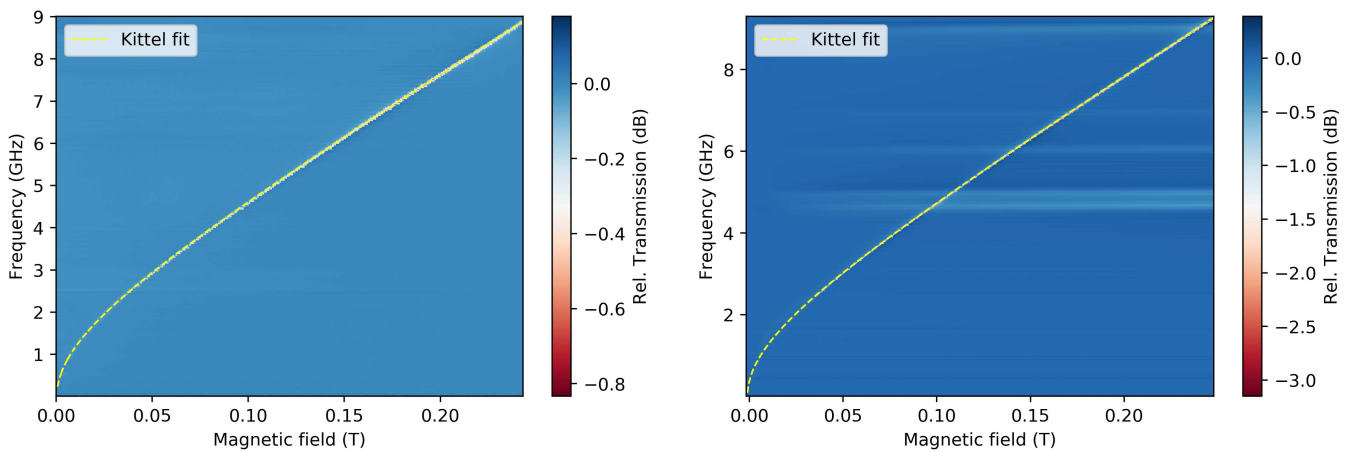
Figure 6.5: [Left] FMR curve for a YIG thin film (0.99 μm) in PCB #1. Kittel fit resulted in values of gyromagnetic ratio of $\gamma = 28.062 \pm 0.058$ GHz/T, saturation magnetization $M_s = 170.9 \pm 1.6$ mT and anisotropy fields $H_a \sim 10^{-4}$ mT. [Right] Using the same sample on PCB #2, the fit resulted in values of $\gamma = 28.957 \pm 0.044$ GHz/T, $M_s = 163.1 \pm 1.2$ mT and $H_a = 1.1 \pm 0.1$ mT. Difference in anisotropy fields could be a result of different sweeping directions on both measurements.

Again, the values obtained match the expected values very well, with special emphasis on the saturation magnetization which is on point with the value of ~ 170 mT (see Table. 6.2).

The main difference between the two fits is seen in the anisotropy fields H_a which is one order of magnitude larger for the latter. This could be explained by the fact that the magnetic field sweep was opposite in both measurements (zero to positive and positive to zero fields, for PCB #1 and #2 measurements respectively) which resulted in two branches being probed: one where the sample starts saturated $(+ \rightarrow 0)$ and other where it starts in a multi domain state and only saturates at higher fields ~ 170 mT $(0 \rightarrow +)$. The difference in gyromagnetic ratios obtained could also be a consequence of this effect.

Regarding non uniform spin waves excited for this sample, the few that got excited

were very close in frequency with the Kittel mode which makes it hard to see on surface plots (Fig. 6.5). However, by taking a close look at the spectrum in different magnetic fields, it is possible to distinguish between these closely spaced spin waves (Fig. 6.6).
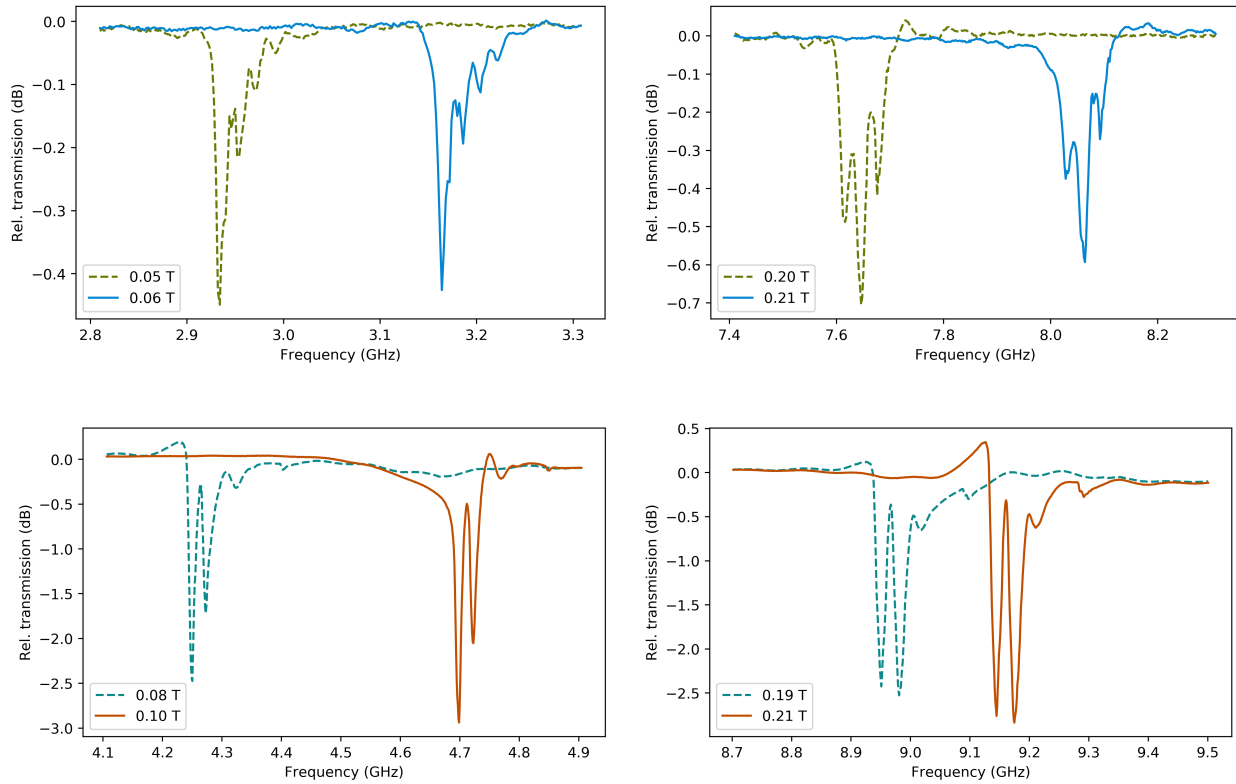
Figure 6.6: [Top, PCB #1] Transmission spectrum at different fields shows few surface and backward volume spin waves excited alongside the Kittel mode. [Bottom, PCB #2] Same spectrum using different PCB excites different spin waves. Specifically, there is one other mode almost as strong as the Kittel.

As will be seen, there was a limitation when trying to fit a Lorenztian profile to the Kittel mode due to the extra overlapping spin waves which created a complex superposition of Lorenztian curves and provided little information about the actual FMR mode itself. Also, while the frequency resolution shown here is low, more careful measurements were done with resolutions down to 100 kHz to get a more accurate representation of the transmission dips and, hence, of the fit parameters.

6.1.1.3   Low field FMR
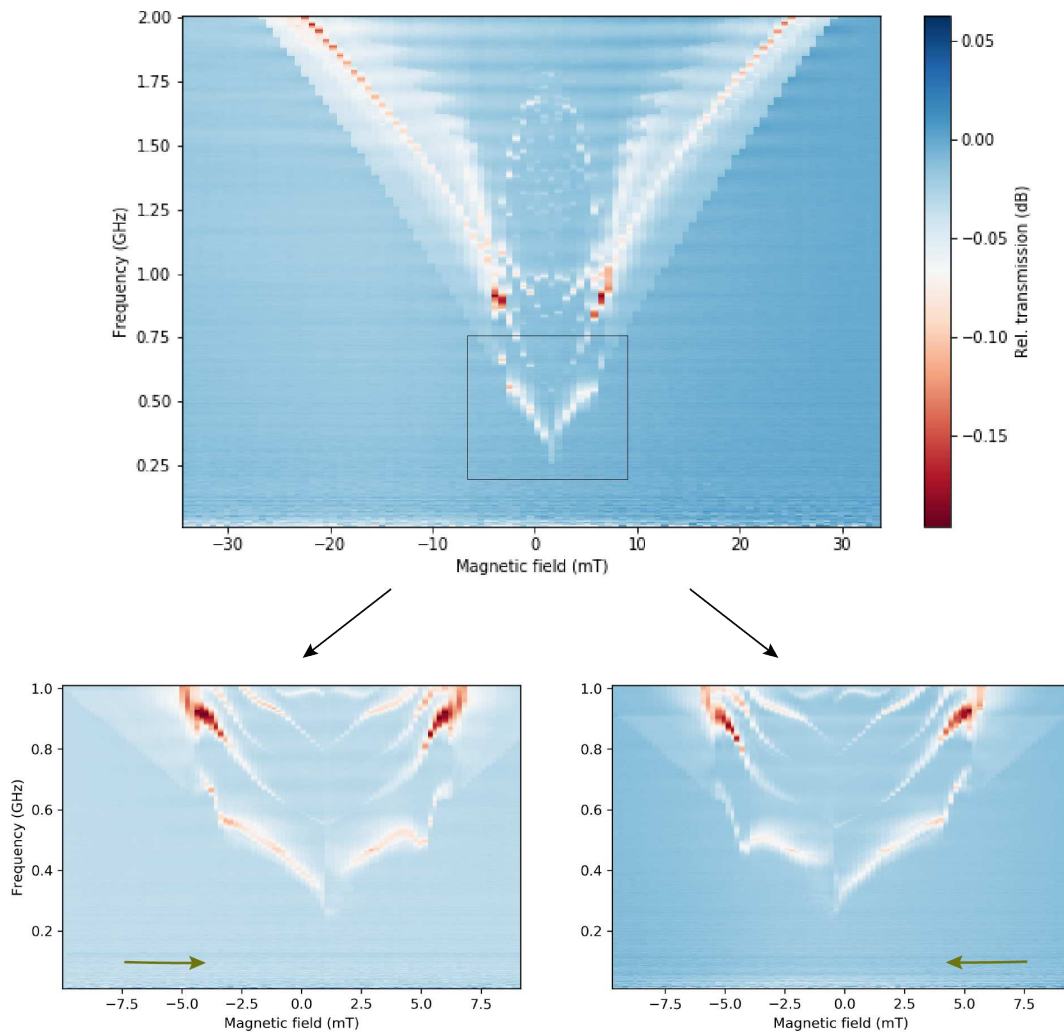
Figure 6.7: [Top] FMR probed at low magnetic fields for a YIG thin film using TMM10 substrate PCB #2. Multidomain structure can be seen at fields below 8 mT. [Bottom] Sweeping magnetic field in different directions results in a small hysteresis behaviour, as well as slight anisotropy.

At low magnetic fields, the sample is not fully magnetized into a single domain which means the multi domain structure creates a complex spectrum of ferromagnetic resonance where each domain resonates at its specific frequency. In practice, this is translated into many FMR curves being present at the same magnetic field (Fig. 6.7), specifically when the field amplitude is below 10 mT. It is also the reason the FMR dip is faint until the fields saturate the magnetization of YIG (Fig. 6.1 and 6.2).

It is also possible to see an hysteresis effect when one sweeps the magnetic field in opposite directions (bottom Fig. 6.7). For instance, when the magnetic field is swept from negative to positive values (left), the magnetization flips (discontinuity)

slightly after zero field, while for the opposite sweep (right) it flips almost exactly at zero field which could be a result of small anisotropies in the film. Overall, these effects are notoriously small in YIG samples due to its small remanence and coercivity fields.

6.1.2 FMR linewidth (Gilbert damping factor)

One of the most important parameters to characterize when studying spin waves in magnetic materials is the Gilbert damping coefficient α (section 3.2.3). This coefficient is related to the distance (and time) spin waves travel in the material before losing phase coherence and vanishing. YIG is known to have the lowest damping factor (meaning spin waves have long lifetimes $\sim$ μs) and, therefore, it is of interest to measure it for these specific samples (sphere and thin film).

To determine the damping factor and the inhomogeneous broadening, the Gilbert damping model was used to fit the linewidth of the Kittel mode (ΔH) as a function of the center frequency (ω), as the magnetic field was increased [20, 44]:

$$\Delta H = \Delta H_0 + 2\alpha\omega/\gamma \tag{6.2}$$

The relation between the magnetic field linewidth ΔH and the frequency linewidth $\Delta\omega \equiv \Delta f$ can be deduced from the Kittel formula. While this conversion is simple for spherical samples ($\Delta f = \gamma/2\pi\,\Delta H$), for thin films, the relation is not linear [20]:

$$\Delta H = \frac{\Delta f}{\gamma P(f)} \tag{6.3}$$

where $P(f)$ is a factor which accounts for the non-spherical shape of the sample. For in-plane magnetized thin films, this factor is given by:

$$P(f) = \sqrt{1 + \left(\frac{\gamma M_s}{4\pi f}\right)^2} \tag{6.4}$$

As the central frequency of the resonance is increased (higher magnetic fields), the less important this correction factor becomes. This effect was seen during data analysis, where data points at lower frequencies changed substantially after the correction term, while higher frequency points remained at practically the same values.

The result of such fit is shown for the YIG sphere and thin film (Fig. 6.8 and Fig. 6.9, respectively). To obtain the best results, PCB #2 was used for the

thin film measurements, while PCB #1 was used for the YIG sphere. Using these transmission lines respectively, the Kittel mode was able to be more separated from overlapping higher order spin waves which were compromising the Lorentzian profile fit. However, at high frequencies and for the thin film, these spin waves still existed and that is the main reason why the fit seems to oscillate around the linear behaviour.
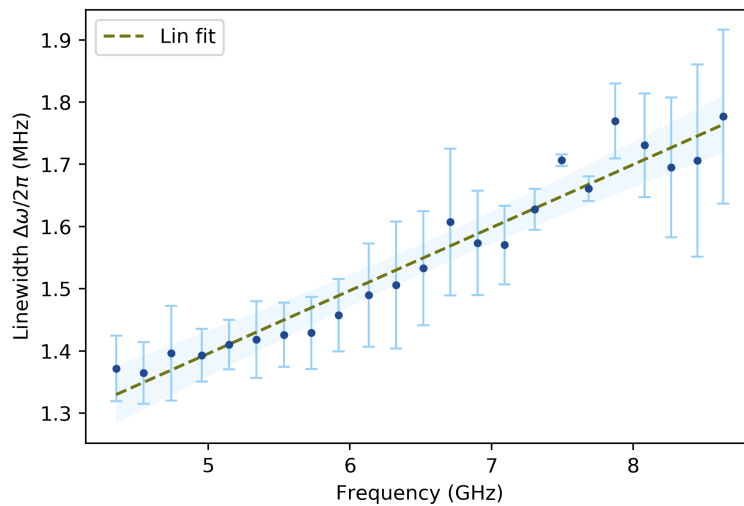
Figure 6.8: Frequency linewidth dependence on resonance frequency for YIG sphere. Fit done to linear function $\Delta\omega = 2\alpha\omega + \omega_0$. Fit results: $\alpha = 0.506\text{e-}04 \pm 0.054\text{e-}04$ and $\Delta\omega_0/2\pi = 0.889 \pm 0.306$ MHz. Shaded region corresponds to a 3σ confidence band for the linear fit.
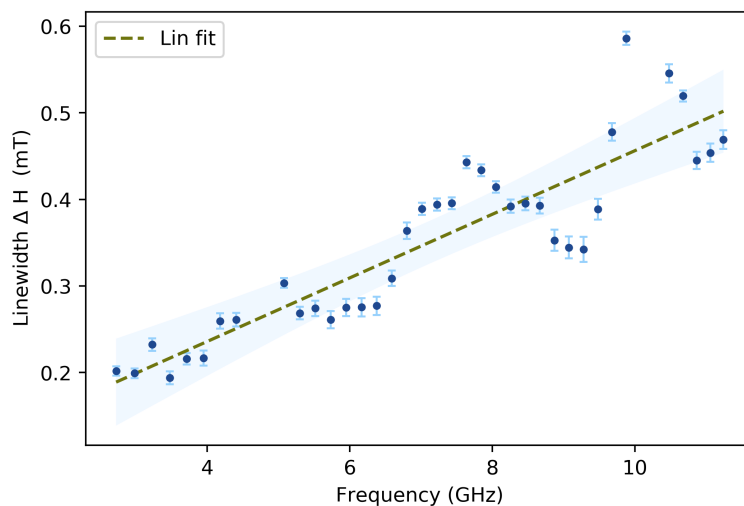
Figure 6.9: Magnetic field linewidth dependence on frequency for YIG thin film. Fit done to equation 6.2 with thin film correction term $P(f)$. Fit results: $\alpha = 5.143\text{e-}04 \pm 0.043\text{e-}04$ and $\Delta H_0 = 0.09 \pm 0.02$ mT . Shaded region corresponds to a 3σ confidence band for the linear fit.

Both fits resulted in Gilbert damping factors close to literature values for YIG

(Table 6.1 and Table 6.2). The error seen in these values is mainly attributed to extra overlapping spin waves which disfigure the Lorentzian profile and worsen the fit parameters. Specifically, it is possible to see the large error bars for the sphere fit which were a result of a slight skewness of the Lorentzian curve, most likely caused by overcoupling to the transmission line. These fits are shown and explained in detail in Appendix A.

6.1.3   Table with results

	Sphere		
	#1	#2	Ref.
$\gamma/2\pi$ (GHz/T)	28.760	28.634	28.025 [46]
α	5.06×10^{-5}	-	4×10^{-5} [45]
$\Delta\omega_0/2\pi$ (MHz)	0.89	-	1.80 [45]

Table 6.1: Parameters extracted from room temperature measurements using two different transmission lines (#1 and #2) for a YIG sphere.

	Film		
	#1	#2	Ref.
$\gamma/2\pi$ (GHz/T)	28.062	28.957	28.025 [46]
M_s (mT)	171	163	170 [2]
α	-	5.14×10^{-4}	$\sim 10^{-4}$ [2, 45]
ΔH_0 (mT)	-	0.09	0.11 [47]

Table 6.2: Parameters extracted from room temperature measurements using two different transmission lines (#1 and #2) for a YIG thin film.

6.2   Cryogenic temperatures

This section is concerned with FMR results obtained at cryogenic temperatures (mainly milliKelvin) using the setup and samples described previously (chapter 5). The main goal was to visualize FMR modes, as well as trying to understand the characteristic linewidth of the samples and their dependence on external field applied. Also, a YIG sample coupled to a superconducting resonator was probed in this temperature regime to study the hybrid structure, namely its coupling strength.

6.2.1   PFIB YIG FMR spectra

6.2.1.1   Sample 1

First sample probed had dimensions $50{\times}50{\times}10$ µm^3 and it was placed over both ground planes of a superconducting NbN CPW transmission line, covering the central conductor. Since FMR signals produced by these samples are so small (e.g. <1 dBm amplitude signals in a -80 dBm baseline), each measurement was configured to get the best resolution possible during each cooldown of the ADR (to mK), for instance, by lowering the VNA's IF bandwidth (hardware averaging) and increasing the number of points taken in field and frequency sweeps. Despite these optimizations, the raw data acquired is still not enough to visualize the FMR signal, so data was post processed, firstly by subtracting background and then by applying a low pass filter which removes some noise due to reflections in the cables.

In this way, a FMR spectrum was obtained at 80 mK (Fig. 6.10 and 6.11), where multiple spin wave modes were excited, as shown in the figures below.
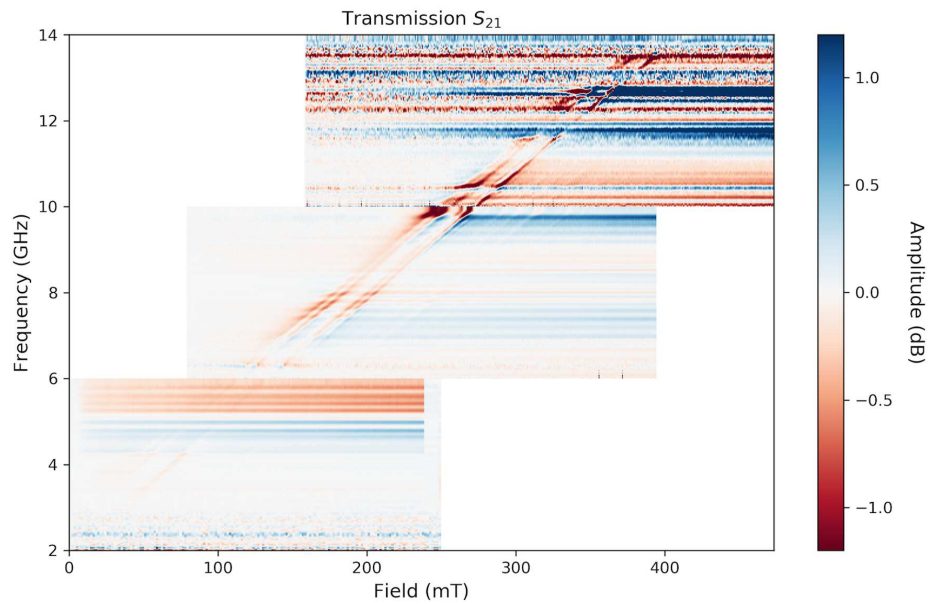
Figure 6.10: FMR spectrum of YIG sample with dimensions $50 \times 50 \times 10 \ \mu m^3$ at 80 mK. Multiple spin wave modes (linear curves) can be seen in the spectrum which are attributed to the shape and size of the sample and its placement over the CPW transmission line. Due to the small signals obtained, data is later processed by correcting the background and applying a low pass filter to remove most noise from the cables (horizontal lines are a result of this processing). Three field sweeps were done, corresponding to the three blocks in the figure, to capture the whole spectrum from zero to very high fields, since the mK temperature in the ADR was not sustainable long enough to measure everything in one sweep (each measurement block corresponds to about 6-7 hours).
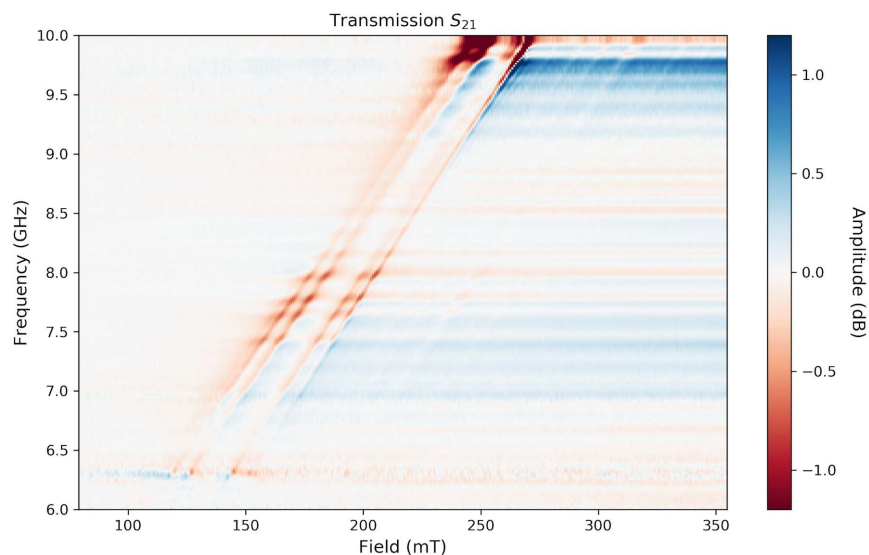
Figure 6.11: Zoom in on FMR spectra, corresponding to the second block in Fig. 6.10. This region provided the best signal to noise ratio and was chosen for a more detailed analysis. It is possible to see four main modes, together in pairs, as well as very weak (< 0.1 dB) modes to the right (faint white lines).

First analysis was done to extract the gyromagnetic ratio $\gamma/2\pi$ from these spin wave modes and the obtained results varied between 27-30 GHz/T, which is to be expected since the fit was done considering a linear relation between frequency and field, despite the Kittel formula for such shape not being linear for all fields, but similar to a thin film (eq. 3.9). Also, only one of the modes corresponds to FMR, therefore the others have slightly different Kittel formulas, resulting in larger deviations of γ from the expected value. It was also not possible to fit the FMR mode at lower fields because the signal was even weaker owing to the sample not being fully magnetized, while at higher fields (i.e. higher frequencies) the measurement system becomes too noisy and the baseline starts to depend heavily on the magnetic field applied.

The multiple spin wave modes observed can be explained by the alternating magnetic field distribution inside the YIG sample, as well as by the dimensions of the sample itself. Since the sample covers both ground planes, its edges are feeling the combined effect of an alternating field that creates inhomogeneous fields inside, therefore exciting higher wavenumber spin waves. The thickness of the sample may also be responsible for creating standing modes which are not presented in this work, but were seen in a detailed analysis of one of the spin wave modes.

More interesting is the study of the FMR linewidth using this sample at cryogenic temperatures. The goal was to follow the treatment in section 6.1.2 and obtain the Gilbert damping factor using the same model and the same linear fit (equation 6.2). Results obtained (Fig. 6.12) were not as conclusive as wanted, with the data not showing a clear evidence of the linear dependence we were looking for. The reason behind the lack of a linear dependence seems to be related to the overlapping of spin waves together with a very weak signal which produces a non-lorentzian shape and the linewidth becomes hard to extract. Nevertheless, the linewidths obtained show a clear increase (almost a factor of ten) from the room temperature YIG linewidths.

This large error comes from the weak signals which sometimes overlap with background features (e.g. stray resonances) and destroy the Lorentzian profile, resulting in a larger linewidth than the sample's intrinsic one. It is also thought that the sample might be in an overcoupling regime, where the loaded quality factor of the resonance (and therefore its linewidth) is much closer to the coupling quality factor than the intrinsic one.
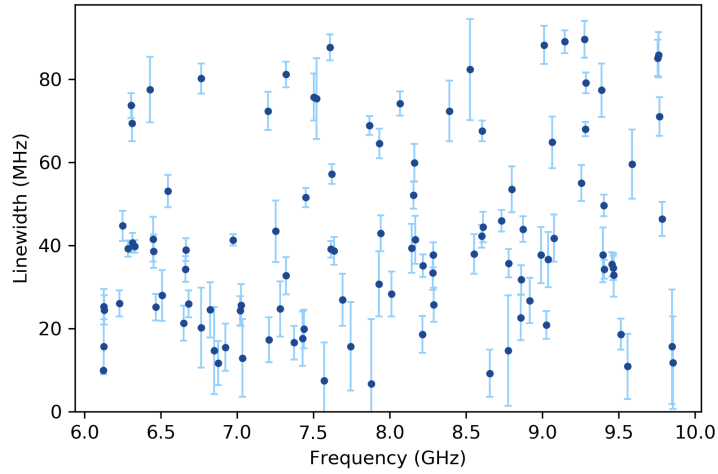
Figure 6.12: Frequency linewidth dependence on FMR frequency for YIG sample 1. Despite the non evident linear dependence, the linewidth is larger when compared to room temperature results for YIG. The origin of this increase is still being investigated.

6.2.1.2 Sample 2

Second sample probed had dimensions $50 \times 10 \times 5$ µm^3 and was placed directly on top of the central conductor of the NbN CPW transmission line. Since the sample was smaller (hence smaller signal), measurement times were even longer which made it very time consuming to probe FMR at mK temperatures. Therefore, FMR data shown below was taken at $\sim$3 K.

With this configuration, a single mode was excited (Fig. 6.13 and 6.14), corresponding to the FMR mode. These results were expected (reason why these dimensions were chosen), specially since the placement over the central conductor meant the sample felt an almost homogeneous field which excited the Kittel mode. By decreasing the thickness in half, the standing modes were also greatly reduced.

Like the previous sample, the gyromagnetic ratio was obtained for this mode (in the 6-10 GHz range) and the value obtained was $\gamma = 26.8 \pm 0.1$ GHz/T. Again, this result deviates slightly from the expected of 28 GHz/T, since the Kittel formula is not linear at all fields, which introduces an error in the value of γ obtained.
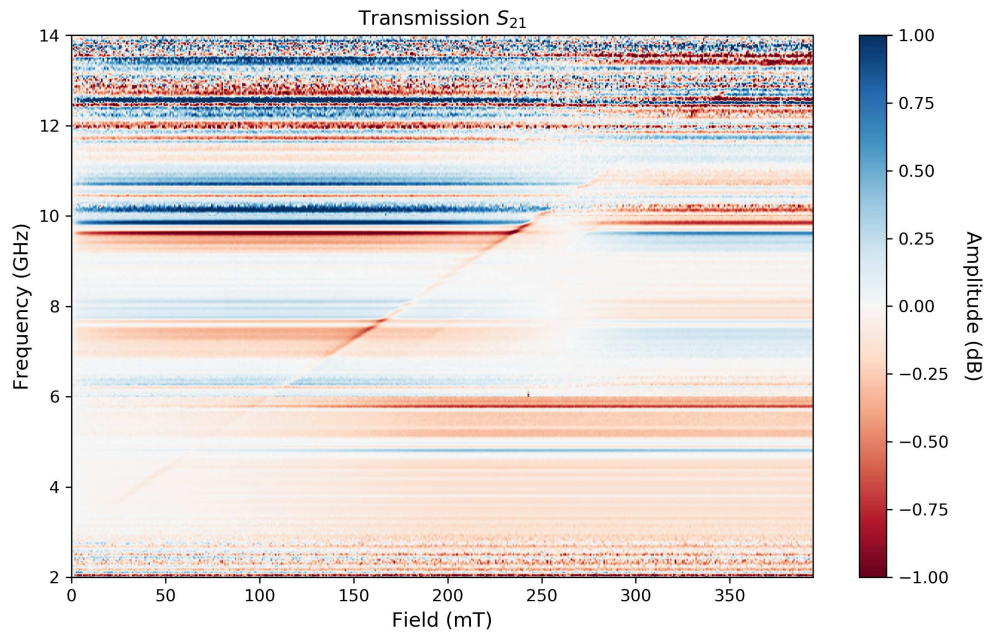
Figure 6.13: FMR spectrum of YIG sample with dimensions $50{\times}10{\times}5$ μm^3 at 3 K. New dimensions and placement resulted in a single spin wave mode (FMR) being excited, while higher order modes are greatly attenuated. Since we were operating at 3 K, there was no time limit and data was taken in a single sweep (12+ hours). Same data processing was done to visualize FMR signals.
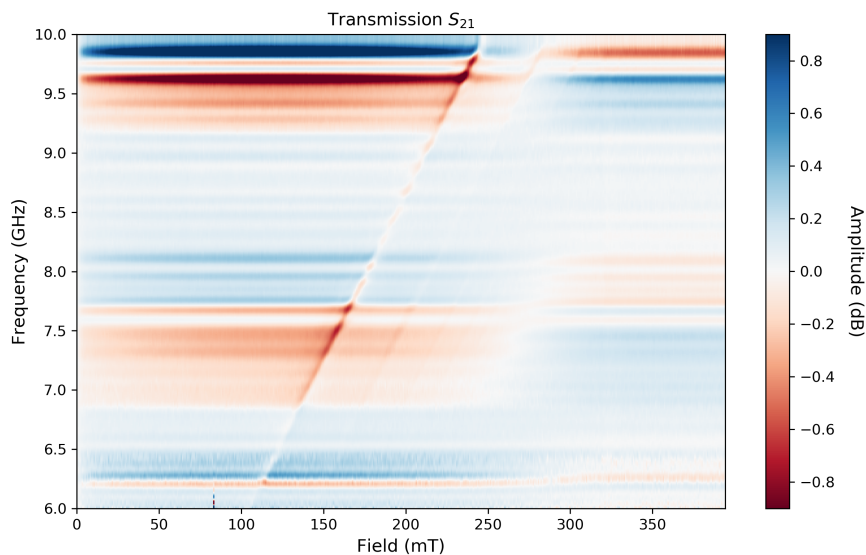
Figure 6.14: Zoom in on FMR spectra, corresponding to the frequency region between 6 and 10 GHz of Fig. 6.13, which provided the best signal to noise ratio. It is possible to see other modes (to the right) which are very attenuated and extremely hard to distinguish.

Regarding the linewidth, same analysis was realized and the results (Fig. 6.15) shows

a better linear dependence, despite the overall linewidths and damping factor being larger. This increase could be explained by a temperature dependence, which would essentially increase the interactions between magnons and other quasiparticles and, as a consequence, greater losses would be observed [6]. New dimensions may also be a result of this increase, namely the new coupling to the feedline could accentuate the overcoupling regime which would also decrease the loaded quality factor.

Further experiments are required to confirm this increase, however one important result is that by decreasing temperatures from 3 K to milliKelvin range, the overall linewidth does not get worse (maybe even improves). This is opposite of what happens with YIG thin films on GGG substrate [5, 37], where the linewidth observed in milliKelvin regime is substantially larger than at few Kelvins. The reason is related to two-level systems in the GGG substrate, which couple to the magnonic modes of YIG at milliKelvin temperatures and act as an unwanted loss channel for the system .
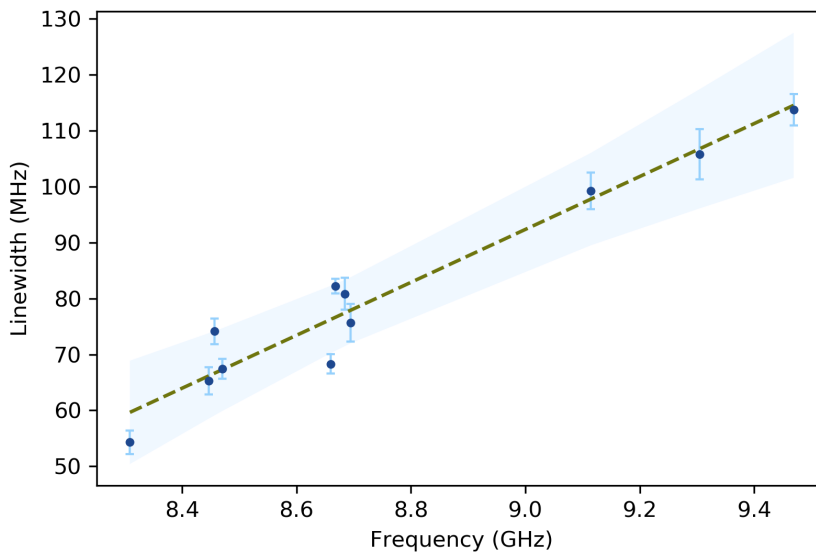
Figure 6.15: Frequency linewidth dependence with FMR frequency for YIG sample 2. Same analysis was carried out which resulted in a damping factor $\alpha = 0.0234 \pm 0.0027$. Fewer points were considered due to difficulties obtaining FMR dips with a well defined Lorenztian profile. This time, linewidth dependence has a clear linear behaviour, but the overall linewidth increased with respect to the previous experiment which could be either related to temperature and/or dimensions of the sample. Shaded region corresponds to a 3σ confidence band for the linear fit.

6.2.2 YIG - NbN resonator hybrid

Previous experiments were concerned with characterizing the magnonic system at cryogenic temperatures, specifically understanding the magnon linewidth and the respective damping factor. These features are of great importance to the field of quantum magnonics [1], where the goal is to create a system where a superconducting qubit and a magnonic system exchange quantum states coherently, with a superconducting resonator acting as an intermediate sub-system.

The final results of this work are concerned with an hybrid system consisting of a $50\times50\times10$ µm^3 YIG sample and a NbN inline $\lambda/2$ superconducting resonator. The resonator was previously designed to have a resonant frequency around 3.80 GHz, consisting of a half wavelength inline meandering layout, with the YIG placed on a straight section, to optimize the homogeneity of the alternate magnetic field near the sample.

Both the first and third harmonic of the resonator were probed to visualize the hybrid system. In theory, inline resonators increase transmission of the microwave signal at resonant frequency, creating a spectrum peak, while notch type resonators work the opposite way and create a dip in transmission (like reflection measurements, which also create dips). With this sample, the resonator behaviour changed quite heavily with the magnetic field swept, creating a Fano type resonance at lower fields (Fig. 6.16) and eventually changing to the inline peak behaviour expected at higher fields (Fig. 6.17).

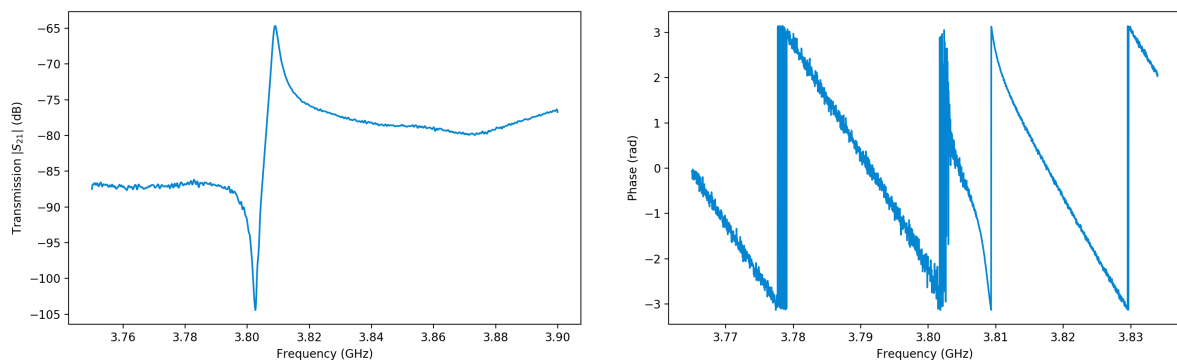Figure 6.16: Resonator probed at the fundamental frequency (3.80 GHz) shows a Fano type resonance, consistent with crosstalk phenomena with other YIG sample on the same chip. Resonance linewidth was determined to be close to 10 MHz. Amplitude (right) and phase (left) data taken with a VNA.
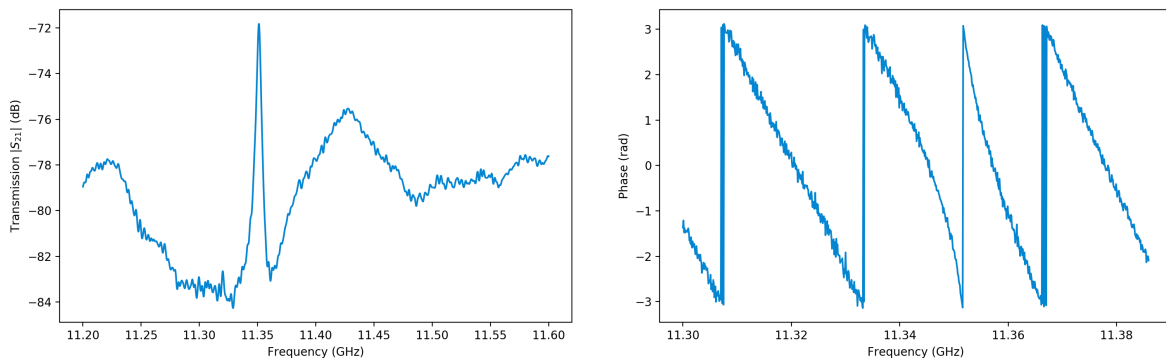
Figure 6.17: Resonator probed at the third harmonic (11.4 GHz) shows the transmission peak, characteristic of inline type resonators. When the resonance condition is met, the impedance either is a minimum (series RLC) or maximum (parallel RLC) which translates to an increase in signal transmission. Amplitude (right) and phase (left) data taken with a VNA.

Due to the large linewidths of these novel, and still unknown, YIG samples, coupling the two systems proved to be quite difficult, especially into the strong regime. In this regime, the two systems would coherently exchange energy with minimal loss and a clear avoided crossing (anticrossing) would appear, transforming the single resonance dip from the resonator into two dips corresponding to the hybrid system.

To better understand the characteristics of the coupling between these two systems, a couple of simulations were realized to show the ideal behaviour of hybrid coupled systems of this type. To do so, the systems simulated were based on a three dimensional system composed of a YIG and a microwave resonator cavity, as in Ref. [48]. Probing reflection spectra, the same coupling regime of our experiment can be seen and compared to the results obtained. Experimental surface plots shown below are accompanied by simulations that show how the parameters of the system influence the type of behaviour seen.

Probing the first harmonic (3.80 GHz), both systems are clearly interacting (Fig. 6.18), but, since the coupling is not strong enough, the magnonic system acts as a loss channel for the resonator photons, effectively enhancing the decay of microwave photons (Purcell regime [48]) and destroying the resonance (e.g. at 67.5 mT). Since we were operating at very low fields (lower than the saturation magnetization of YIG), one of the reasons for the small coupling could be related to the sample being in multi domain magnetic state, which would decrease both the signal strength and the linewidth.
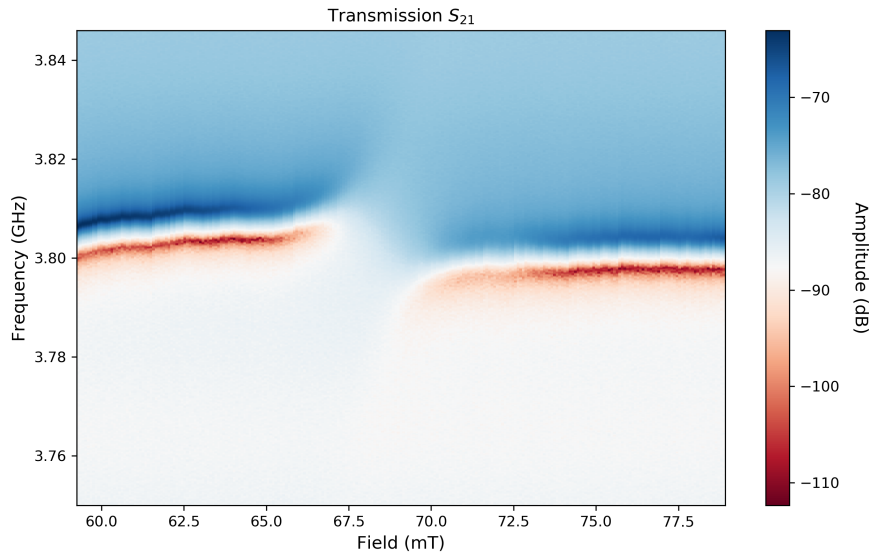
Figure 6.18: Eigenmodes of YIG sample and NbN resonator's first harmonic (3.80 GHz) create an avoided crossing where the two system couple and exchange energy. Due to the large linewidths observed for the YIG sample, it was not possible to observe a strong regime. Instead, the data shows a regime where the YIG system works as loss channel for microwave photons, destroying the resonance phenomenon when the hybrid system is created.
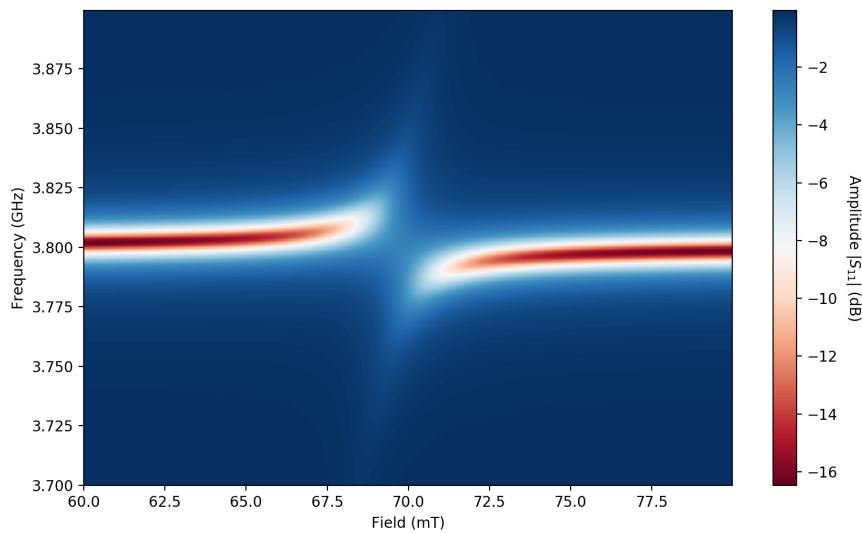
Figure 6.19: Simulated reflection spectrum of three dimensional system of a magnonic and resonator system showing the avoided crossing typical of hybridization. Parameters were chosen as to simulate the weak coupling of the experimental results (Fig. 6.18): resonator linewidth $\kappa_r/2\pi = 5$ MHz, magnon linewidth $\kappa_m/2\pi = 50$ MHz, coupling strength $g/2\pi = 35$ MHz and external coupling of resonator to feedline $\kappa_{r0} = 2$ MHz.

Comparing to the simulated results (Fig. 6.19), we see it is possible to recreate this

behaviour theoretically, just by understanding the coupling regime and its relation to the resonator and magnon linewidths. To get a strong coupling regime, the coupling strenght should be larger than both linewidths ($g \gg \kappa_{r,m}$). By defining the coupling strength to be almost equal to the largest linewidth, we obtain the previous results.

The third harmonic of the resonator (~ 11.4 GHz) was also probed to understand the impact of a fully magnetized sample on the hybrid system (Fig. 6.20).
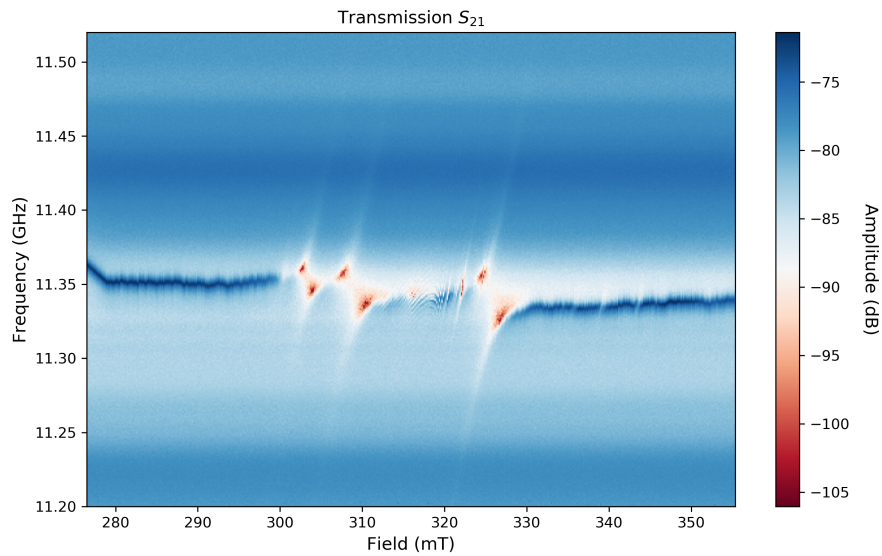
Figure 6.20: Third harmonic of NbN resonator probed together with the YIG system show three different anticrossings, corresponding to three different spin wave modes hybridizing with the resonator. Coupling regime was still not strong enough to show the clear splitting, however it is easier to follow the resonator shifting up (from lower fields) and down (from higher fields).
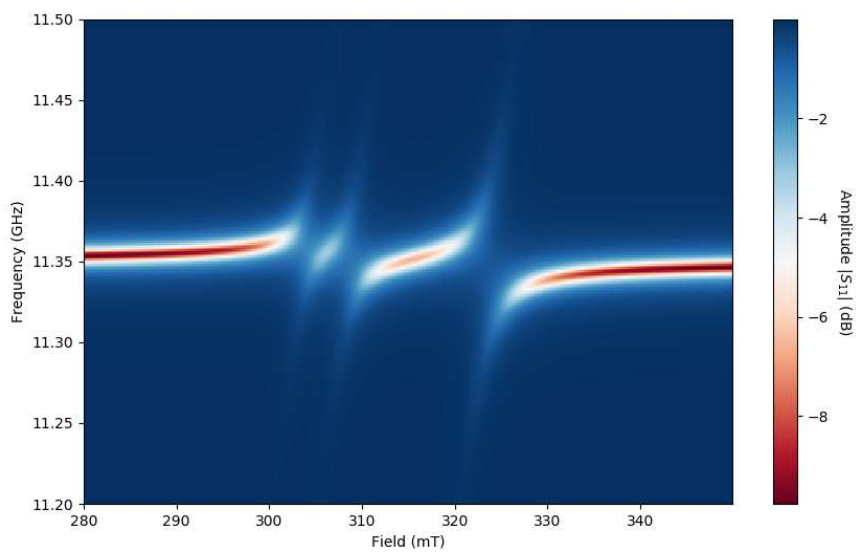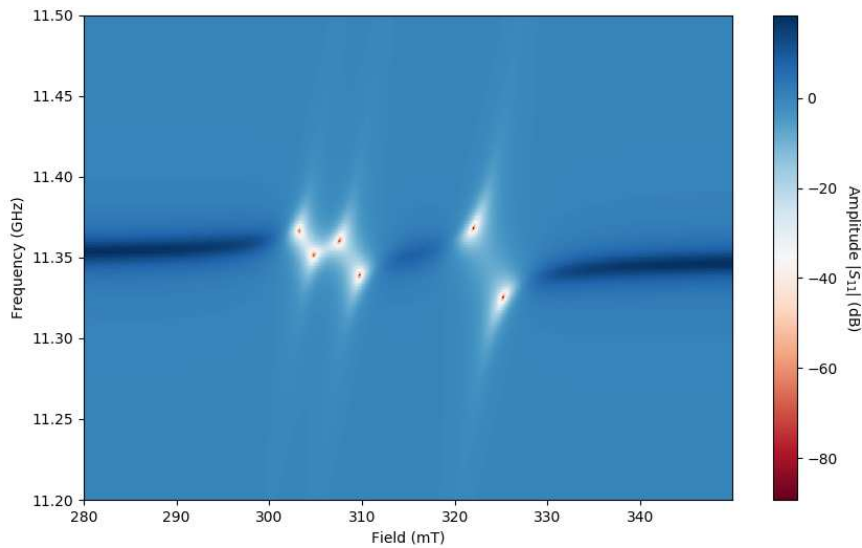
Figure 6.21: Simulation of reflection spectrum probed near third harmonic of resonator with three distinct spin wave modes, where top and bottom correspond to two different external coupling strengths κ_{r0} (1 and 9 MHz, respectively). By increasing the resonator external coupling (bottom), it is possible to replicate the hybrid regime obtained experimentally (Fig. 6.20).

Results show that the anticrossing is slightly stronger at these frequencies and fields, despite still not reaching the strong regime desired. Other modes also appear which correspond to the previously mentioned non-uniform spin waves excited (section 6.2.1). The change between peak (normal inline resonance) into a strong dip at the avoided crossings is surprising and is still a topic being studied more carefully [7]. Nevertheless, this change can be simulated (bottom Fig. 6.21) by increasing the external coupling strenght between the inline resonator and the feedline, in a regime of weak coupling. Future experiments with new sample dimensions and placement still need to be done in order to take better conclusions about hybrid systems using these novel YIG samples.

Chapter 7

Conclusions and Future Work

In this work, YIG ferromagnetic spin systems were studied in detail for two distinct temperature regimes. At room temperature, a YIG sphere and thin film were placed over a microstrip transmission line in a FMR-VNA setup to obtain characteristics of the samples such as the gyromagnetic ratio, Gilbert damping factor and magnetic anisotropies. At cryogenic temperatures, and being the main focus of the work, novel YIG samples fabricated using PFIB technique were placed on a superconducting CPW transmission line to probe the FMR spectrum, as well as placed on a superconducting NbN CPW half wavelength resonator to study the hybridization of magnonic and photonic systems and creation of "avoided crossings".

Room temperature results were consistent with previous experiments done with these shapes of YIG. Ferromagnetic resonant frequency follows the Kittel formula for ellipsoidal shapes such as spheres and thin films, where the fundamental physical difference follows from the distinct demagnetizing factors, characteristic of every shape. Both formulas fitted with great accuracy to the FMR spectrum obtained experimentally, resulting in a low error value for the gyromagnetic ratio and saturation magnetization of YIG thin films. By changing the width and the substrate material used for the microstrip transmission line, it was possible to excite and observe higher order non uniform spin waves, which are the focus of the study in the field of magnonics.

Cryogenic temperature results show the FMR characteristics of novel YIG samples, fabricated using a focused ion beam technique, with great potential for future quantum magnonic experiments. Two dimensions of cuboid shaped samples were studied, along with their placement on the transmission line. By decreasing the thickness it was seen that fewer standing modes appeared, consistent with the hypothesis that shorter volumes correspond to higher resonant frequencies, which would appear well

above the frequency range of our experiments (<20 GHz). By decreasing the width, we were able to place the sample on the central conductor of the transmission line, which resulted in essentially one mode being excited (FMR), due to the greater homogeneity of the alternating magnetic field.

For both these samples, a linewidth study was performed which showed their limitation by the shape, dimensions and coupling regime to the transmission line. Regarding temperature dependences, linewidths seem to decrease slightly from 3 K to 80 mK, albeit this difference could be a result of uncertainties in the data. Further experiments need to be done in order to confirm this hypothesis. Nonetheless, it is safe to assume the linewidth does not get worse by lowering to milliKelvin, which is exactly the problem with YIG thin films on GGG substrates.

A hybrid system consisting of the same YIG samples and a half wavelength superconducting resonator was probed, at mK, with the goal of observing strong coupling between the two systems. Due to the high damping factors of the YIG samples, it was not possible to observe this regime, but instead a weak coupled hybrid system where the magnonic system acts as a decay channel for the microwave photons in the resonator.

Future work aim at improving this characteristic by trying different structures and couplings, to reach a damping factor closer to the room temperature YIG thin films. By lowering the linewidths down to a value close to room temperature YIG, the hybrid system will be tested once more to visualize a strong coupling regime. Different structures of resonators and their resonant frequencies may also be studied, namely notch type, to optimize parameters such as external coupling. The end goal for these experiments is adding a superconducting qubit to the circuit and begin experimenting with a full quantum magnonic system.

Appendices

Appendix A

Lorentzian fitting

The shape of FMR curves obtained in this work is mostly consistent with a Lorentzian homogeneous profile of spectral line broadening [20, 49]. This type of profile is defined by the distribution function:

$$L(\nu) = \frac{2A}{\pi\gamma_0} \frac{1}{1 + 4\left((\nu - \nu_0)/\gamma_0\right)^2} \tag{A.1}$$

where, for this work, A represents the area under the curve, γ_0 is the full width at half maximum (linewidth) and ν_0 is the center frequency of the peak. Using this function, fitting was realized using a least squares method to determine the best parameters (namely, the linewidth) (Fig. A.1).
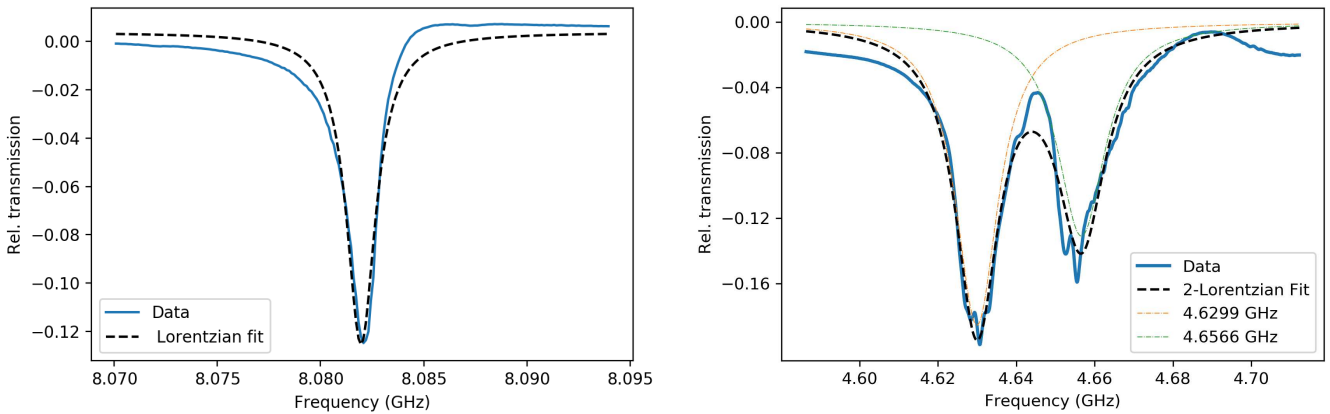

Figure A.1: (Left) Transmission spectrum of YIG sphere at H=315 mT using microstrip #1 (Right) Transmission spectrum of YIG film at H=100 mT using microstrip #2. Best fits to Lorentzian functions are shown using equation A.1.

When multiple spin waves were present near the FMR mode, fitting multiple Lorentzian

shaped curves provided the best result and the FMR mode was identified as the curve with strongest dip and lower frequency (Fig. A.2).
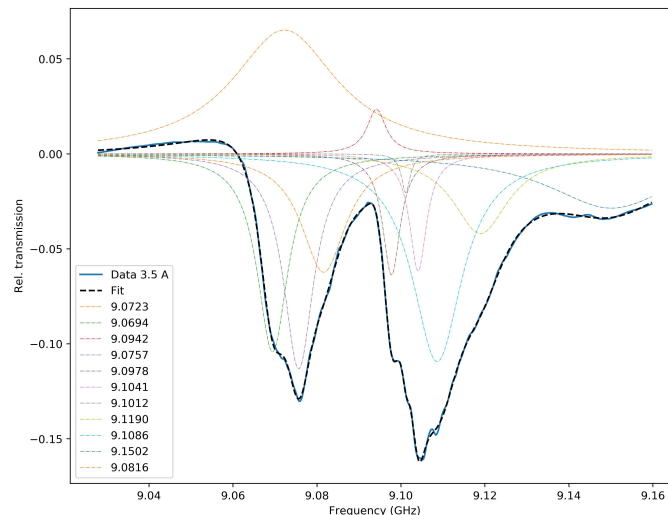
Figure A.2: Transmission spectrum of YIG film at H=240 mT for microstrip #2 shows the rich magnetostatic spin-wave spectrum around the Kittel mode (frequency span of ~ 60 MHz). Lorentzian profiles were fit to get as many spin-wave modes as possible. As the magnetic field gets stronger, more overlapping spin waves disfigure the Kittel mode, like in this figure, which worsens the linewidth linear dependency with frequency.

In both spectra, it was possible to identify a feature which corresponded to an slight increase in transmission right before or after resonance transmission dips (Fig. A.1, A.2). This feature has been shown to be related to overcoupling of the resonator with the transmission line, where energy is mainly lost to the coupled line and the loaded quality factor decreases.

Specifically for the YIG sphere, one way to compensate for this behaviour was to fit using a skewed Lorentzian version, which introduces asymmetry by describing the width γ as a sigmoidal function of frequency [49]:

$$\gamma(\nu) = \frac{2\gamma_0}{1 + e^{a(\nu - \nu_0)}} \tag{A.2}$$

where a is a quantity related to how much the curve shifts from symmetric behaviour. Despite being a better fit (Fig. A.3), the linewidth obtained also includes the behaviour of the extra resonance, therefore the linewidth linear dependence becomes less evident (Fig. A.4).
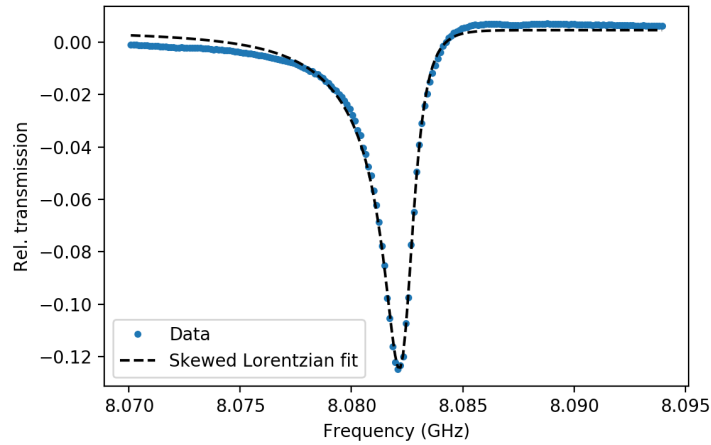
Figure A.3: Transmission spectrum for YIG sphere. Fit done using a skewed Lorentzian function shows a better match between data and fit.
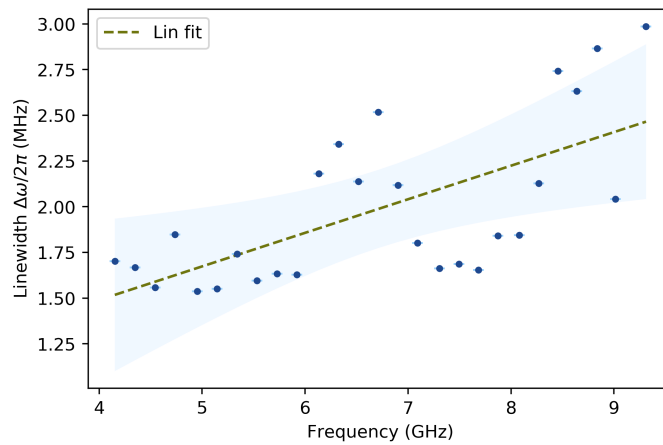
Figure A.4: Frequency linewidth dependence on resonance frequency for YIG sphere. Skewed Lorentzian profile was used to fit the Kittel mode which resulted in a much lower error, but decrease in linearity (cf. Fig. 6.8). Fit done to linear function $\Delta\omega = 2\alpha\omega + \omega_0$. Fit results: $\alpha = 0.918\text{e-}04 \pm 0.210\text{e-}04$ and $\Delta\omega_0/2\pi = 0.755 \pm 0.289$ MHz. Shaded region corresponds to a 3σ confidence band for the linear fit.

Appendix B

ADR Solenoid calibration

Following the procedure described at the end of section 5.3, transmission data was acquired in a traditional electron paramagnetic resonance experiment. The goal was to extract the calibration parameter of the magnet which approximately converts the current provided to the magnetic field inside the solenoid and compare it to the expected value. First step required a background removal using data from a frequency sweep at zero current/field as the background. Afterwards, the wanted signal from the paramagnetic resonance of DPPH becomes clear, despite still being weak (left fig. B.1). The calibration parameter is extracted from the slope, using the well known electron gyromagnetic ratio, such that multiple fits with different frequency ranges were performed to obtain an average value. Final result was found to be closer to 79 mT/A with an uncertainty of $\pm$ 1 mT/A. Comparing to the expected value ($\sim$ 83 mT/A), it is surprisingly very close, taking into account the manual winding process and the imperfections associated with it.

Figure B.1: (Left) Filtered transmission data with background removed showing a faint resonance linear curve (Right). Resonance dip for different currents (data shifted vertically for better visualization). Values of transmission $|S_{21}|$ in arbitrary units.

Appendix C

Qkit

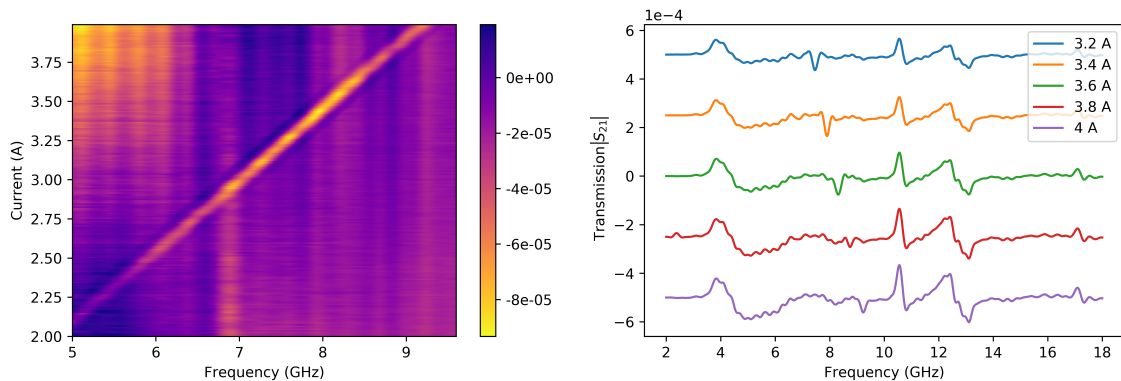In the experiments described in the main text, the software Qkit was used to acquire and analyse the data from the instruments. Qkit is a quantum measurement suite developed for Python programming language and its source code can be found at: https://github.com/qkitgroup/qkit.

Qkit's strength relies on the ability to gather all digital instruments used in the experimental setup (mostly microwave and low frequency electronics) and creating a way to acquire data and visualize it in real time, while all data is being stored in an hierarchical data storage (HDF) type file. Typical experiments include visualization of 1, 2 and 3 dimensional plots (for example, frequency and power sweeps in the VNA). This software also includes classes with data fitting functionalities such as circle fits for microwave resonators or coupling strength extraction for 2D avoided level crossing plots.

The goal of this appendix is to describe the basic operation and flow, as well as to document the implementation of new instrument drivers which connect the physical instruments with the software virtual environment.

C.1   Base structure and flow

The core of Qkit consists of three fundamental blocks that work together to acquire and display the data in a graphical user interface (GUI). These blocks can be classified as:

- Instrument block - contains all the classes related to the instruments, such as the drivers, which implement the communication (two way communication between Qkit and instrument, using write and query instructions) and acquire

the data directly from the physical instrument through a specific communication protocol (e.g. TCP/IP, GPIB, Serial, SPI).

- Measurement block - contains methods and classes to control the measurement procedure and, therefore, manages the acquisition of data from the instruments. Options available include spectroscopy, as well as time-domain measurements. The data acquired is saved to an HDF file.

- GUI block - creates the graphical interface used to plot and present the data from the HDF file. The interface is also complemented with real time analysis tools such linear, offset and norm corrections.

The block diagram shown below (Fig. C.1) gives a detailed overview of the structure and flow of Qkit, starting from the initialization of the module up to the point where the physical device is communicating with it.

The initialization is called on a python environment by importing the global module (import qkit) after which the remaining essential modules will load. Examples of such modules include a logger which starts a log for error and program execution management and debugging, multiple configuration modules which implement or disable user-specific options (e.g. where to write data, adicionar qui) and finally the qkit_start module which starts the instruments and flow control of the program.

Once the qkit environment is started, one can start measurement methods to begin extracting data from the instruments through the driver module of each one. The data generated by the measurements is stored in a HDF file format which is read by a GUI to plot and analyse the experimental data obtained.

Python environment
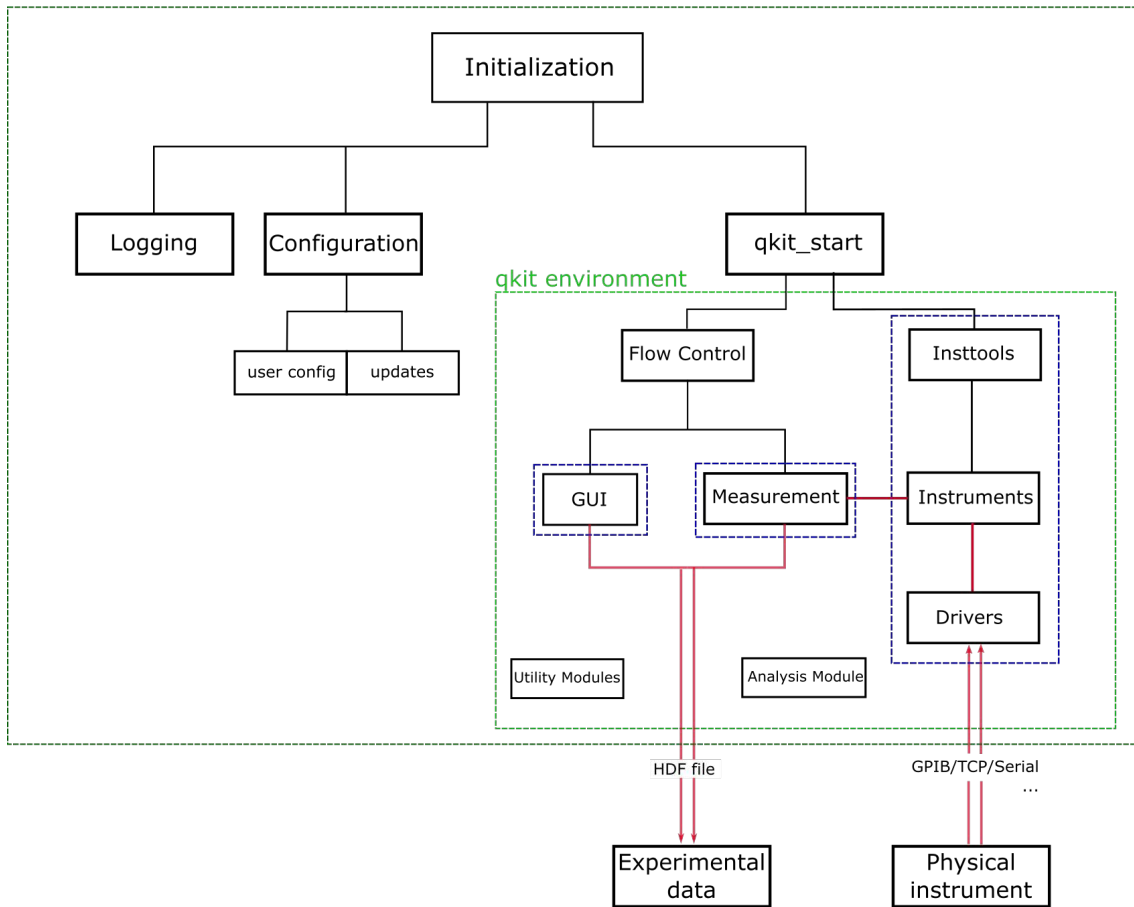
Figure C.1: Qkit's block diagram with main components highlighted in blue referring to instrument, measurement and GUI blocks. Red lines represent the flow of physical data between the instrument and the data output from qkit.

C.2 Instrument drivers

One of great aspects of Qkit is the ability to add new instruments to the experiment and having it integrated in a single software by writing a driver module which becomes part of Qkit's environment and can communicate with the physical instrument.

The integration of the driver module is done through the Instrument block mentioned before. In this block, there are two general modules which contain all the instrument objects and can manipulate them (common to all instruments) and one driver module (specific to each instrument):

- `instrument_tools` is responsible to create the instrument's python object (through the __init__ constructor defined in the corresponding driver module) which can be called by any other Qkit module. This module also contains a

dictionary which stores the active instruments created in a single session of an experiment.

- `instrument_base` contains the class Instrument which acts as a wrapper to the actual driver. This class implements the setters and getters of the parameters of the instrument. These parameters are also added through this class in the driver module.

- `instrument_driver` (e.g. `Anritsu_VNA_MS4642B`) implements the communication protocol used for the instrument (physical interfaces include GPIB, USB, Ethernet, Serial, ...) usually by defining write and query instructions which are sent to the device using the protocol defined. It is also possible to define methods in the driver which can be added by the `Instrument` class to be used in Qkit environment.

During this work, new drivers were written and implemented for different instruments (such as Hall probe sensors, Digital-to-Analog Converters, ...) to integrate the whole experiments within Qkit. A general procedure to create new drivers starts with searching on the instrument's documentation for remote control or remote procedure calling functionalities to find out the interface standard used, as well as the instructions defined to write and query the instrument.

In the driver module itself, a Python class needs to be created specific to the instrument. This class should contain:

- Constructor method (`__init__`) to initialized the module and set configurations for the device. The communication protocol should be initiated here (e.g. start a pyvisa object if the instrument's interface is supported), however it is also possible to defined a side function to initialize it later from any module. Parameters to be manipulated by the driver (e.g. voltage, current, frequency sweeps, power output, ...) are also defined in the constructor through the `add_parameter` method from the `Instrument` class inside the constructor.

- `do_set` and `do_get` methods for each parameter defined, depending on whether the parameter is set/get only or supports both actions.

- Side methods/functions (optional) can be implemented in the module and added to Qkit environment through the use of `add_function` method from the `Instrument` class.

References

[1]D. Lachance-Quirion, Y. Tabuchi, A. Gloppe, K. Usami, and Y. Nakamura, "Hybrid quantum systems based on magnonics", Applied Physics Express **12**, 070101 (2019).

[2]A. A. Serga, A. V. Chumak, and B. Hillebrands, "YIG magnonics", Journal of Physics D: Applied Physics **43**, 264002 (2010).

[3]V. V. Kruglyak, S. O. Demokritov, and D. Grundler, "Magnonics", Journal of Physics D: Applied Physics **43**, 264001 (2010).

[4]A. D. Karenowska, A. V. Chumak, A. A. Serga, and B. Hillebrands, "Magnon spintronics", in *Handbook of spintronics*, edited by Y. Xu, D. D. Awschalom, and J. Nitta (Springer Netherlands, Dordrecht, 2016), pp. 1505–1549.

[5]S. Kosen, A. F. van Loo, D. A. Bozhko, L. Mihalceanu, and A. D. Karenowska, "Microwave magnon damping in yig films at millikelvin temperatures", APL Materials **7**, 101120 (2019).

[6]I. Boventer, M. Pfirrmann, J. Krause, Y. Schön, M. Kläui, and M. Weides, "Complex temperature dependence of coupling and dissipation of cavity magnon polaritons from millikelvin to room temperature", Phys. Rev. B **97**, 184420 (2018).

[7]P. Baity, J. Barbosa, et al. (2020) in preparation.

[8]D. M. Pozar, *Microwave Engineering*, 4th ed. (John Wiley & Sons, 2012).

[9]*Keysight Technologies - Understanding the Fundamental Principles of Vector Network Analysis*, (2019) https://literature.cdn.keysight.com/litweb/pdf/5965-7707E.pdf (visited on Nov. 18, 2019).

[10]*Rhode & Schwarz - Fundamentals of Vector Network Analysis*, (2019) https://www.signalintegrityjournal.com/ext/resources/White-papers-App-notes/Vector-Network-Analyzer-Fundamentals-Primer.pdf (visited on Nov. 18, 2019).

[11] S. Probst, F. B. Song, P. A. Bushev, A. V. Ustinov, and M. Weides, "Efficient and robust analysis of complex scattering data under noise in microwave resonators", Review of Scientific Instruments **86**, 024706 (2015).

[12] M. Tinkham, *Introduction to Superconductivity: Second Edition* (Dover Publications, 2004).

[13] J. Zmuidzinas, "Superconducting microresonators: physics and applications", Annual Review of Condensed Matter Physics **3**, 169–214 (2012).

[14] J. M. Sage, V. Bolkhovsky, W. D. Oliver, B. Turek, and P. B. Welander, "Study of loss in superconducting coplanar waveguide resonators", Journal of Applied Physics **109**, 063915 (2011).

[15] B. A. Mazin, "Microwave kinetic inductance detectors", PhD thesis (California Institute of Technology, 2005).

[16] J. M. Martinis, K. B. Cooper, R. McDermott, M. Steffen, M. Ansmann, K. D. Osborn, K. Cicak, S. Oh, D. P. Pappas, R. W. Simmonds, and C. C. Yu, "Decoherence in josephson qubits from dielectric loss", Phys. Rev. Lett. **95**, 210503 (2005).

[17] H. Wang, M. Hofheinz, J. Wenner, M. Ansmann, R. C. Bialczak, M. Lenander, E. Lucero, M. Neeley, A. D. O'Connell, D. Sank, M. Weides, A. N. Cleland, and J. M. Martinis, "Improving the coherence time of superconducting coplanar resonators", Applied Physics Letters **95**, 233508 (2009).

[18] S. V. Vonsovskii, *Ferromagnetic resonance; the phenomenon of resonant absorption of a high-frequency magnetic field in ferromagnetic substances*, English, 1st ed. (Pergamon Press Oxford, New York, 1966).

[19] I. Neudecker, G. Woltersdorf, B. Heinrich, T. Okuno, G. Gubbiotti, and C. Back, "Comparison of frequency, field, and time domain ferromagnetic resonance methods", Journal of Magnetism and Magnetic Materials **307**, 148–156 (2006).

[20] S. S. Kalarickal, P. Krivosik, M. Wu, C. E. Patton, M. L. Schneider, P. Kabos, T. J. Silva, and J. P. Nibarger, "Ferromagnetic resonance linewidth in metallic thin films: comparison of measurement methods", Journal of Applied Physics **99**, 093909 (2006).

[21] X. Zhang, C. Zou, L. Jiang, and H. X. Tang, "Superstrong coupling of thin film magnetostatic waves with microwave cavity", Journal of Applied Physics **119**, 023905 (2016).

[22] G. Nahrwold, J. M. Scholtyssek, S. Motl-Ziegler, O. Albrecht, U. Merkt, and G. Meier, "Structural, magnetic, and transport properties of permalloy for spintronic experiments", Journal of Applied Physics **108**, 013907 (2010).

References

[23] J. Van Vleck, *The theory of electric and magnetic susceptibilities*, International series of monographs on physics (University press, 1932).

[24] S. Blundell, *Magnetism in condensed matter*, Oxford Master Series in Condensed Matter Physics (OUP Oxford, 2001).

[25] C. Kittel, "On the theory of ferromagnetic resonance absorption", Physical Review **73**, 155–161 (1948).

[26] L. D. Landau and E. M. Lifshitz, *"on the theory of the dispersion of magnetic permeability in ferromagnetic bodies"*, Phys. Z. Sowjet., vol. 8, pp. 153–169, 1935. In L. D. Landau, Collected Papers. ed. by D. ter Haar. Gordon and Breach, New York, 1967, p. 101.

[27] T. L. Gilbert, "A phenomenological theory of damping in ferromagnetic materials", IEEE Transactions on Magnetics (2004) `10.1109/TMAG.2004.836740`.

[28] V. Baryakhtar, "Phenomenological description of relaxation processes in magnets", Zhurnal Ekspretimentalnoi I Teoreticheskoi Fiziki **87**, 1501–1508 (1984).

[29] U. Atxitia, D. Hinzke, and U. Nowak, "Fundamentals and applications of the landau–lifshitz–bloch equation", Journal of Physics D: Applied Physics **50**, 033003 (2016).

[30] R. J. Runge, "Approximate solutions of the modified bloch equations for low magnetic fields", Journal of Mathematical Physics (1962) `10.1063/1.1703869`.

[31] F. Bloch, "Nuclear induction", Physica (1951) `10.1016/0031-8914(51)90068-7`.

[32] R. Codrington, J. Olds, and H. Torrey, "Paramagnetic resonance in organic free radicals at low fields", in Phys. rev. Vol. 95, 2 (1954), pp. 607–608.

[33] P. W. Anderson, "The concept of spin-lattice relaxation in ferromagnetic materials", Phys. Rev. **88**, 1214–1214 (1952).

[34] T. Kasuya and R. C. LeCraw, "Relaxation mechanisms in ferromagnetic resonance", Phys. Rev. Lett. **6**, 223–225 (1961).

[35] M. J. Hurben and C. E. Patton, "Theory of two magnon scattering microwave relaxation and ferromagnetic resonance linewidth in magnetic thin films", Journal of Applied Physics **83**, 4344–4365 (1998).

[36] L. Berger, "A simple theory of spin-wave relaxation in ferromagnetic metals", Journal of Physics and Chemistry of Solids **38**, 1321–1326 (1977).

[37] M. Pfirrmann, I. Boventer, A. Schneider, T. Wolz, M. Kläui, A. V. Ustinov, and M. Weides, "Magnons at low excitations: observation of incoherent coupling to a bath of two-level systems", Phys. Rev. Research **1**, 032023 (2019).

[38] L. R. Walker, "Magnetostatic modes in ferromagnetic resonance", Phys. Rev. **105**, 390–399 (1957).

[39] *Data Sheet TMM®Thermoset Microwave Materials*, TJA1043, Rev. 3, Rogers Corporation (Apr. 2013).

[40] V. Cherepanov, I. Kolokolov, and V. L'vov, "The saga of YIG: Spectra, thermodynamics, interaction and relaxation of magnons in a complex magnet", Physics Reports **229**, 81–144 (1993).

[41] F. Pobell, "Refrigeration by adiabatic demagnetization of a paramagnetic salt", in *Matter and methods at low temperatures* (Springer Berlin Heidelberg, Berlin, Heidelberg, 1992), pp. 148–157.

[42] A. de Waele, "Pulse-tube refrigerators: principle, recent developments, and prospects", Physica B: Condensed Matter **280**, 479–482 (2000).

[43] S. Krinner, S. Storz, P. Kurpiers, P. Magnard, J. Heinsoo, R. Keller, J. Lütolf, C. Eichler, and A. Wallraff, "Engineering cryogenic setups for 100-qubit scale superconducting circuit systems", EPJ Quantum Technology **6**, 2 (2019).

[44] T. D. Rossing, "Resonance linewidth and anisotropy variation in thin films", Journal of Applied Physics **34**, 995–995 (1963).

[45] S. Klingler, H. Maier-Flaig, C. Dubs, O. Surzhenko, R. Gross, H. Huebl, S. T. B. Goennenwein, and M. Weiler, "Gilbert damping of magnetostatic modes in a yttrium iron garnet sphere", Applied Physics Letters **110**, 092409 (2017).

[46] NIST, *CODATA value: electron gyromagnetic ratio*, (2018) `https://www.physics.nist.gov/cgi-bin/cuu/Value?gammaebar` (visited on Nov. 20, 2019).

[47] C. Hauser, T. Richter, N. Homonnay, C. Eisenschmidt, M. Qaid, H. Deniz, D. Hesse, M. Sawicki, S. G. Ebbinghaus, and G. Schmidt, "Yttrium iron garnet thin films with very low damping obtained by recrystallization of amorphous material", Scientific reports **6**, 20827–20827 (2016).

[48] X. Zhang, C.-L. Zou, L. Jiang, and H. X. Tang, "Strongly coupled magnons and cavity microwave photons", Phys. Rev. Lett. **113**, 156401 (2014).

[49] A. L. Stancik and E. B. Brauns, "A simple asymmetric lineshape for fitting infrared absorption spectra", Vibrational Spectroscopy **47**, 66–69 (2008).